Three-dimensional simulation of thermodynamics on confined turbulence in a large-scale CME-flare current sheet

Jing Ye,[1,2,3] John C. Raymond,[4] Zhixing Mei,[1,2] Qiangwei Cai,[5,2] Yuhao Chen,[1,6] Yan Li,[1,2] and Jun Lin[1,2,6]

[1]Yunnan Observatories, Chinese Academy of Sciences, P.O. Box 110, Kunming, Yunnan 650216, People's Republic of China
[2]Yunnan Key Laboratory of Solar Physics and Space Science, P.O. Box 110, Kunming, Yunnan 650216, People's Republic of China
[3]Yunnan Province China-Malaysia HF-VHF Advanced Radio Astronomy Technology International Joint Laboratory, Kunming, Yunnan 650216, People's Republic of China
[4]Smithsonian Astrophysical Observatory, 60 Garden Street, MS 15, Cambridge, MA 02138, USA
[5]Institute of Space Physics, Luoyang Normal University, Luoyang, Henan 471934, People's Republic of China
[6]University of Chinese Academy of Sciences, Beijing 100049, People's Republic of China

ABSTRACT

Turbulence plays a key role for forming the complex geometry of the large-scale current sheet (CS) and fast energy release in a solar eruption. In this paper, we present full 3D high-resolution simulations for the process of a moderate Coronal Mass Ejection (CME) and the thermodynamical evolution of the highly confined CS. Copious elongated blobs are generated due to tearing and plasmoid instabilities giving rise to a higher reconnection rate and undergo the splitting, merging and kinking processes in a more complex way in 3D. A detailed thermodynamical analysis shows that the CS is mainly heated by adiabatic and numerical viscous terms, and thermal conduction is the dominant factor that balances the energy inside the CS. Accordingly, the temperature of the CS reaches to a maximum of about 20 MK and the range of temperatures is relatively narrow. From the face-on view in the synthetic Atmospheric Imaging Assembly 131 $\mathring{A}$, the downflowing structures with similar morphology to supra-arcade downflows are mainly located between the post-flare loops and loop-top, while moving blobs can extend spikes higher above the loop-top. The downward-moving plasmoids can keep the twisted magnetic field configuration until the annihilation at the flare loop-top, indicating that plasmoid reconnection dominates in the lower CS. Meanwhile, the upward-moving ones turn into turbulent structures before arriving at the bottom of the CME, implying that turbulent reconnection dominates in the upper CS. The

Corresponding author: Jing Ye
yj@ynao.ac.cn

spatial distributions of the turbulent energy and anisotropy are addressed, which show a significant variation in the spectra with height.

Keywords: Magnetohydrodynamical Simulation — Coronal Mass Ejection – Turbulence – Magnetic reconnection

1. INTRODUCTION

Coronal Mass Ejections (CMEs) are the most energetic events in the solar system, and they cause major changes of the large-scale magnetic structures in the corona. Various empirical and analytical models are proposed for the initiation and evolution of CMEs, such as Catastrophe model (Lin & Forbes 2000; Lin et al. 2001), Breakout model (Antiochos et al. 1999; MacNeice et al. 2004),Titov & Démoulin (1999) model, Photospheric converging model (Amari et al. 2003; Zhao et al. 2017), Flux emergence model (Archontis et al. 2004), and Tether-cutting model (Moore et al. 2001; Jiang et al. 2021). In the process of the solar eruption, the closed magnetic field is highly stretched by the loss of equilibrium and a plate-like reconnection region, namely current sheet (CS), forms between the two magnetic fields of opposite polarity, and magnetic reconnection (MR) occurs in the CS (Mikic & Linker 1994; Forbes & Lin 2000; Lin et al. 2002). Therefore, a long CS is always expected to appear in the major eruption. With one end anchored on the rising flux rope (FR), the CS forms a low pressure area where both magnetic field and plasma from the background are pushed into the CS, as reconnection inflows. In other words, the reconnection process in the plate-like CS is externally driven by the rising FR and the reconnection inflows in the third dimension.

A sufficiently fast reconnection rate is required to support a successful solar eruption (Lin 2002). The mechanism responsible for driving the fast magnetic reconnection in the CS is an ongoing research topic. The Sweet-Parker model only describes a slow reconnection with a long and thin diffusion region (Sweet 1958; Parker 1957), while Petschek model is often used to explain the fast magnetic reconnection process by introducing a single X-type reconnection region (Petschek 1964). Furthermore, plasmoid instabilities (Loureiro et al. 2007; Bhattacharjee et al. 2009) and turbulence (Strauss 1988; Lazarian et al. 2012; Lazarian et al. 2020) play key roles in efficient diffusion in the reconnecting CS. The linear theory for the tearing mode (Furth et al. 1963) suggests that the CS becomes unstable to tearing mode as the aspect ratio exceeds 2π. And Shen et al. (2011) suggest that plasmoid instabilities take place in the solar flares only if the Lundquist number exceeds a critical value of $S \approx 10^4$. The non-linear instability tears the global CS into many small-scale pieces with many plasmoids transferring the magnetic energy from large to small scales. At the same time, merging magnetic islands create an inverse cascade (Fermo et al. 2010). The cascades result in power-law spectra in the flux and size distributions with indices near -2 (Bárta et al. 2011; Shen et al. 2013). The well-developed turbulence in the CS is mainly generated by plasmoid instability in 2D, and the global CS is filled with the diffusion region due to the appearance of plasmoids (Ye et al. 2019; Xie et al. 2022). However, 3D and 2D turbulence are fundamentally different in the process of MR (Eyink et al. 2011). The theoretical work of Lazarian & Vishniac (1999) predicts a fast reconnection speed in the presence of weak turbulence, which is numerically verified in 3D by Kowal et al. (2009). And the turbulent meandering of magnetic field lines has been shown numerically to induce a strong violation of magnetic flux freezing (Eyink et al. 2013). It is shown by Kowal et al. (2017, 2020); Beresnyak (2017) that 3D turbulence develops spontaneously in the reconnection layer, and it is not a collection

of 2D magnetic loops. Lazarian et al. (2020) also suggest that plasmiod reconnection dominates in 2D, while turbulent reconnection is more prominent in 3D. On the other hand, Nishida et al. (2013) made an effort to extend the 2D model of solar flares to a 3D model, and conclude that the plasmoid-induced reconnection theory is still valid in 3D cases. Dong et al. (2022) recently performed 3D simulations of MHD turbulence at a large magnetic Reynolds number of $R_m = 10^6$, and they provide direct evidence that plasmoids can play a role for forming the turbulent energy spectra with an index of -2.2. Thus the mechanism of magnetic reconnection in the realistic turbulent CS is still poorly understood.

Many observations suggest that fragmented and turbulent structures exist to enable the reconnection in the CME-flare CS (Lin et al. 2007; Liu 2013; Lin et al. 2015; Li et al. 2018; Cheng et al. 2018; Lee et al. 2020). Patel et al. (2020) further accomplish a statistical study of plasmoids in the CS of the CME eruption on September 10, 2017 using extreme-ultraviolet (EUV) and white-light coronagraph images. For the same event, Warren et al. (2018) observe the formation and evolution of the hot CS, consistent with the 2D numerical work of Ye et al. (2020). It has been also observed by Hanneman & Reeves (2014); Innes et al. (2014); Cai et al. (2019) that a distributed plasma structure of about 10 MK, namely supra-arcade fan (SAF), exists above the post-flare loops. And the motion of supra-arcade downflows (SADs) contributes significantly to the plasma heating of the SAF (Reeves et al. 2017; Samanta et al. 2019). The formation of the SAF and the SAD were recently shown to be related to the turbulent region above the flare loops by simulations (Cai et al. 2021; Shen et al. 2022; Ruan et al. 2023). Additionally, Mei et al. (2017) compared the 3D CS formed during the FR eruption with that in 2D models, which are very similar in the planar cut view, but they only considered an isothermal solar atmosphere. Reeves et al. (2019) investigate the plasma heating in the CS using 3D simulations considering thermal conduction and radiative cooling mechanisms, but the eruption is not very energetic, with maximum plasma temperatures about only $\sim 3 - 5$ MK. However, the direct numerical study on thermodynamics of the large-scale CS and plasmoids in 3D CMEs are still limited.

In this paper, we perform full 3D MHD simulations based on Titov & Démoulin (1999) model to study the CME-driven reconnection process. Adaptive mesh refinement (AMR) is utilized to achieve the high resolution grid around the 3D CS, in order to capture the evolution of fine structure within. In section 2, the analytical solution for the initial configuration and numerical setups are described. Section 3 shows the numerical results of the global and local evolution. Lastly, we give the discussion and conclusions in Section 4.

2. NUMERICAL DESCRIPTION

The governing MHD equations used in our simulations are described in Cartesian geometry as follows:

$$\frac{\partial \rho}{\partial t} + \nabla \cdot (\rho \mathbf{v}) = 0 \tag{1}$$

$$\frac{\partial e}{\partial t} + \nabla \cdot [(e + P^*)\mathbf{v} - (\mathbf{v} \cdot \mathbf{B})\mathbf{B}]$$
$$= \rho \mathbf{g} \cdot \mathbf{v} + \nabla \cdot [\eta \mathbf{B} \times (\nabla \times \mathbf{B}) - \mathbf{F}_C] \tag{2}$$

$$\frac{\partial (\rho \mathbf{v})}{\partial t} + \nabla \cdot [\rho \mathbf{v}\mathbf{v} - \mathbf{B}\mathbf{B} + P^*\mathbf{I}] = \rho \mathbf{g} \tag{3}$$

$$\frac{\partial \mathbf{B}}{\partial t} = \nabla \times (\mathbf{v} \times \mathbf{B} - \eta \nabla \times \mathbf{B}) \tag{4}$$

$$P^* = P + \frac{\mathbf{B} \cdot \mathbf{B}}{2} \tag{5}$$

$$P = \rho T \tag{6}$$

where ρ is the plasma mass density, $\mathbf{v}$ is the flow velocity, P is the thermal pressure, η is the magnetic resistivity, $\mathbf{B}$ and $\hat{\mathbf{B}}$ are the magnetic field and the associated unit vector, $\gamma = 5/3$ is the ratio of specific heats, $\mathbf{g}$ is the gravitational acceleration, and $e = P/(\gamma - 1) + \rho \mathbf{v}^2/2 + \mathbf{B} \cdot \mathbf{B}/2$ is the total energy density. The Spitzer model for thermal conduction (Spitzer 1962) is included in Eq.(2) in the form of $\mathbf{F}_C = -\kappa_{||}(\nabla T \cdot \hat{\mathbf{B}})\hat{\mathbf{B}} - \kappa_{\perp}(\nabla T - (\nabla T \cdot \hat{\mathbf{B}})\hat{\mathbf{B}})$. The parallel and perpendicular coefficients $\kappa_{||}, \kappa_{\perp}$ are the same as given in Ye et al. (2021). Particularly, thermal conduction must saturate as the temperature gradient becomes too large, and the heat flux is limited to the saturated flux of Cowie & McKee (1977) (See Appendix). All variables presented here are dimensionless. The normalization units are $L_0 = 5 \times 10^9$ cm, $n_0 = 10^{10}$ cm^{-3} and $T_0 = 10^6$ K for length, number density and temperature, respectively. Thus, we have the characteristic values $\rho_0 = 1.673 \times 10^{-14}$g cm^{-3}, $B_0 = 5.89$ G, $P_0 = 2.76$ g cm^{-1}s^{-2}, $v_A = 128.5$ km s^{-1} and $t_0 = 389.15$ s for mass density, magnetic strength, gas pressure, velocity and time. To complete the equations, the divergence-free condition $(\nabla \cdot \mathbf{B} = 0)$ needs to be satisfied at any evolution time.

The gravitational acceleration deceases with the height along the z-axis, given in the dimensionless form by $\mathbf{g} = -\rho_0 L_0/P_0 g_0 \hat{\mathbf{z}}/(1 + zL_0/R_{\odot})^2$. Here, we have the gravitational acceleration constant near the solar surface $g_0 = 2.74 \times 10^4$ cm s^{-2}, the solar radius $R_{\odot} = 6.961 \times 10^{10}$ cm, and the unit vector $\hat{\mathbf{z}}$ in z-direction. In order to hold naturally the line-tied condition at the bottom of the simulation box, we adopted a two-layer gravitationally stratified atmosphere including the chromosphere and the corona. The initial temperature distribution is given simply by

$$T(z) = \begin{cases} T_{chr}, & \text{for} \quad 0 \leq z \leq h_{chr}, \\ T_{cor}, & \text{for} \qquad z > h_{chr}, \end{cases} \tag{7}$$

where $T_{chr} = 0.01$ is the chromosphere temperature, $T_{cor} = 1$ is the corona temperature, and $h_{chr} = 0.4$ is the top of the chromosphere. We note that the initial temperature distribution is not continuous at the low altitude. The thermal conduction could change the gravitationally stratified layer once the simulations start. Since the associated conduction time at the low layer is much longer than the simulation time, the plasma evolution in higher coronal regions won't be significantly affected in the

later phases. Then we have the associated gas pressure distribution due to hydrostatic equilibrium:

$$P(z) = \begin{cases} p_{chr} \exp\left[\dfrac{1}{\lambda T_{chr}} \dfrac{-z}{1 + zL_0/R_\odot}\right], & \text{for} \quad 0 \le z \le h_{chr}, \\ p_{cor} \exp\left[\dfrac{1}{\lambda T_{cor}} \dfrac{(-z + h_{chr})}{(1 + zL_0/R_\odot)(1 + h_{chr}L_0/R_\odot)}\right], & \text{for} \quad z > h_{chr}, \end{cases} \tag{8}$$

with

$$p_{chr} = p_{cor} \exp\left[\frac{1}{\lambda T_{chr}} \frac{h_{chr}}{1 + h_{chr}L_0/R_\odot}\right], \quad \lambda = \frac{2k_B T_0}{m_H g_0 L_0}. \tag{9}$$

Here, $k_B = 1.38 \times 10^{-23}$erg K^{-1} is the Boltzmann constant, $m_H = 1.67 \times 10^{-24}$ g is the mass of the hydrogen atom, and p_{cor} is the gas pressure set at the height $z = h_{chr}$.

The initial magnetic configuration is similar to the T & D model (Titov & Démoulin 1999; Török et al. 2004), which consists of three components. The first component, denoted by B_I, comes from a pre-existing flux rope of major radius R, carrying a uniformly distributed ring current I of a minor radius a. The second one, denoted by B_q, is created by a pair of magnetic sources with the distance L at the depth $z = -d_1$ under the photosphere ($z = 0$). The two sources of charge $\pm q_1$ are located symmetrically to the axis of the ring to mimic the active region. The detailed formulae for B_I and B_q can refer to Titov & Démoulin (1999). The third one, denoted by B_t, represents a dipole source of strength q_2 buried at $z = -d_2$ at the origin of xy-plane, in order to allow the magnetic strength to decay with the square of the height. Following the work by Mei et al. (2020), the associated magnetic potential vector reads as

$$\mathbf{A}_t = \frac{q_2}{(x^2 + y^2 + (z + d_2)^2)^{3/2}} \begin{pmatrix} z + d_2 \\ 0 \\ -x \end{pmatrix} \tag{10}$$

On the assumption of a thin enough flux rope (i.e. $a << R$), we can treat the global and internal equilibrium almost independently (Isenberg et al. 1993) . The global equilibrium in an axisymmetric system is reduced to the balance between the Lorentz Forces caused by the curvature of the tube axis and interaction of the background magnetic field B_q at the given strength $\pm q_0$ with the ring current I, which gives the equilibrium current

$$I = \frac{8\pi q_0 LR(R^2 + L^2)^{-3/2}}{\ln(8R/a) - 5/4}. \tag{11}$$

Since this work mainly focuses on the detailed evolution after the major eruption, we start the simulation from a non-equilibrium state by setting $q_1 = 0.7q_0$, in order to have an immediate eruption.

On the other hand, the internal equilibrium of the flux rope is realized by the balance between the inward force from the poloidal magnetic field and the outward force from the thermal pressure and magnetic pressure from the toroidal field (Mei et al. 2018). Hence, we have the explicit expression for the gas pressure within the flux rope:

$$P = P_m + (1 - \alpha)\frac{I^2}{4\pi^2 a^2}\left(1 - \frac{r_a^2}{a^2}\right), \quad \text{for} \quad r_a \le a, \tag{12}$$

with

$$r_a = \sqrt{x^2 + (r_\perp - R)^2}, \\ r_\perp = \sqrt{y^2 + (z - d_1)^2}. \tag{13}$$

Note that α is the ratio of the thermal pressure to magnetic pressure, and P_m denotes the background pressure obtained from Eq.(8). Reusing the symbol of the line current I_0 in Titov & Démoulin (1999), the internal toroidal field can be written as

$$B_t = \frac{I_0}{2\pi}\left[\sqrt{\frac{2\alpha I^2}{a^2 I_0^2}\left(1 - \frac{r_a^2}{a^2}\right) + \frac{1}{R^2}} + \sqrt{y^2 + (z + d_1)^2} - \frac{1}{R}\right], \quad r_a \leq a. \tag{14}$$

In this way, we only need to adjust the value of I_0 to make the external field derived from Eq.(10) and the internal field of Eq.(14) the same at the surface of the flux rope (Mei et al. 2018). In addition, the flux rope is supposed to carry the cold plasma from the chromosphere (Mackay & van Ballegooijen 2009), so the temperature within is set to $T = 0.02$ for $r_a \leq a$. Therefore, the initial density distribution is eventually obtained by Eq.(6).

The simulation box is defined in 3D as $(x, y, z) \in [-4, 4] \times [-4, 4] \times [0, 12]$, and the root grid size is $80 \times 80 \times 120$. For the study of 3D small-scale structures in the CS, it is necessary to carry out the appropriate mesh refinement techniques to save computational sources. Practically, the static mesh refinement (SMR) of maximally 3 levels is utilized before the computation starts: level 1 for $(x, y, z) \in [-0.8, 0.8] \times [-1.6, 1.6] \times [0, 5]$, level 2 for $(x, y, z) \in [-0.4, 0.4] \times [-0.8, 0.8] \times [0, 4.5]$, level 3 for $(x, y, z) \in [-0.2, 0.2] \times [-0.6, 0.6] \times [0.5, 4]$. And the adaptive mesh refinement (AMR) of 5 levels is activated in the region of $[-0.4, 0.4] \times [-0.5, 0.5] \times [0.5, 5]$ around the CS for $t \geq 0.4$ and the finest cell size corresponds to a physical length of 156.25 km. The essential parameters for our model are given as $L = 0.4$, $R = 1.2$, $a = 0.2$, $d_1 = 0.1$, $d_2 = 1.2$, $q_0 = 40.75$, $q_2 = 2.92$ and $\alpha = 0.997$. The gas pressure at $z = h_{chr}$ is $p_{cor} = 1$, which gives the plasma $\beta \approx 0.15$ at the bottom of the corona. The normalized resistivity is set as $\eta = 10^{-5}$, resulting in a diffusion coefficient $\eta_c = \eta L_0 v_A = 6.425 \times 10^{11}$ cm^{2}s^{-1} in cgs units.

The boundary conditions included are similar to the 2D case of Ye et al. (2021). That is the line-tied condition at the bottom boundary $z = 0$ formalized by Shen et al. (2018), while the open conditions are used for the other 5 boundaries allowing the plasma to enter or exit freely the simulation box. The full 3D simulations are performed by the MPI-parallelized AMR code "MPI-AMRVAC" (Keppens et al. 2012; Xia et al. 2018) using the Godunov style finite volume method in general. Additionally, we choose the Harten-Lax-van Leer approximate Riemann solver (Harten 1983) together with a third-order asymmetric flux limiter (Koren 1993) to capture the shock structures and a three-step Runge-Kutta time solver. The anisotropic heat flux is solved by the SuperTimeStepping method (Meyer et al. 2012). We have completed two runs with and without thermal conduction as listed in table 1. The Appendix shows that the temperature distribution for Run A is much overestimated (larger than 100 MK) leading to the very low density inside the CS, while the distributions for Run B are more consistent with observations. Conduction is a dominant factor that balances the energy inside the CS. It also turns out, from our simulations, that Run B shows the large-scale CS with more flux tube structures appearing than Run A. In order to better study the turbulent features of the CS, the detailed analyses in the next section are all based on the results from Run B.

Table 1. Simulation parameters for Run A and B.

	root grid	AMR levels	Thermal conduction
Run A	$80 \times 80 \times 120$	5	No
Run B	$80 \times 80 \times 120$	5	Yes

To compare with observations, the synthetic extreme ultraviolet (EUV) emissions are produced by the forward modeling code FoMo (v3.4, Van Doorsselaere et al. (2016)), taking into account contribution functions from the CHIANTI atomic database (Del Zanna et al. 2015). The spatial resolution of the EUV images is the same as the observations, with a pixel corresponding to 435 km at 131 $\mathring{A}$ passband.

3. SIMULATION RESULTS

3.1. *Global evolution*

Figure 1 shows the formation and multi-scale processes of the CS by the current isosurface $|J| = 50$ following the erupted flux rope (FR) in 3D configurations. A close-up look for the detailed dynamical evolution in the CS is presented in the corresponding animation from $t = 0$ to $t = 2.2$. We roughly calculate the effective resistivity $\eta_e = V_{\text{in}}\delta$ to be about at 2.38×10^{14} cm^{2}s^{-1} at $t = 1.42$, where $\delta \approx 4.7 \times 10^7$ cm is the minimum full width of the CS, and $V_{\text{in}} \approx 50.7$ km/s is the reconnection inflow velocity near the middle of the CS. Then the resulting Lundquist number is estimated by $S = L_c V_c / \eta_e \approx 1.5 \times 10^4$, with $L_c \approx 2RL_0 = 1.2 \times 10^{10}$ cm the characteristic FR length and $V_c \approx 2904.1$ km/s the Alfvén velocity near the magnetic sources. This indicates that the use of the computational grid in our simulations is fine enough to trigger plasmoid instabilities shown by the small flux tubes in the CS. Panel (a) displays the pre-existing filament carrying the ring current and no CS is formed at the beginning. At $t = 0.52$ in panel (b), the CS fan between the flare and FR is well built up and the first plasmoid marked by the red box appears. The flux tube-like structures of the plasmoid are locally constructed by the twisted field lines. Then at $t = 0.96$ in panel (c), the CS is extremely stretched in the middle, and the field lines of the FR crossing the z-axis evolve into a clockwise rotation. At this time, the buffer region under the FR seems more turbulent than the CS, which has only a few blobs near its flanks. Later at $t = 1.42$ in panel (d), blobs continue to appear simultaneously close to the flare loop-top and undergo merging or splitting, which makes the internal CS structures quite chaotic. One can find also that the field lines of the FR in the middle rotate at a significant angle with respect to the yz-plane, which forms a complex geometry of the CS instead of a flat sheet. Lastly at $t = 2.0$ in panel (e), the general CS system becomes completely turbulent at higher altitudes.
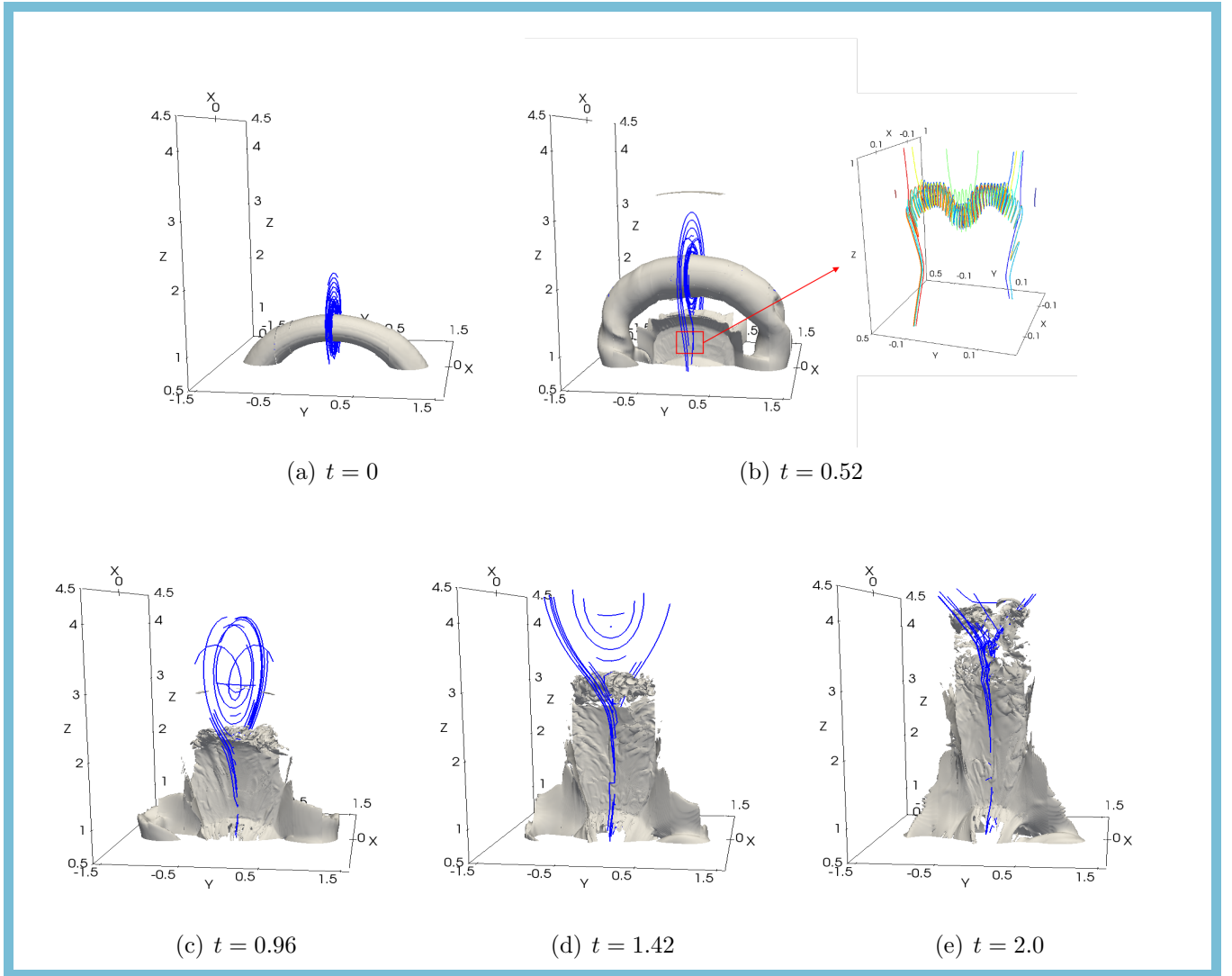
Figure 1. Snapshots of the global evolution of current density and magnetic fields at different times. The structures of the current sheet are shown by the current isosurface with value $|J| = 50$ in white. The blue solid lines are magnetic fields crossing the z-axis. The colors are used in the right panel in (b) for the better visualization of different magnetic fields for the first plasmoid marked in the red box in the left panel. An animation of the detailed evolution inside the 3D CS is available for the entire simulation time.

In Figure 2, we plot the spatio-temporal diagram along the z-axis passing the origin using the highest level 5 of AMR, in order to follow the detailed evolution of the CS driven by the ejected FR. In panel (a), one can easily distinguish the fast shock by the shape change and the FR of denser material from the distribution of density in height. The principal X-line (PX), where magnetic reconnection takes place the fastest, is located always close to the lower tip of the CS, causing the energy partition asymmetric. As we can see, the FR undergoes an acceleration phase for $t \lesssim 0.52$ and then moves upward with a speed of about 338.5 ± 12.8 km/s. Many blobs seen as fluctuations in density are generated due to instabilities in the CS, and propagate bi-directionally. The reconnection upflows collide with the FR to form a dense buffer region underneath. Unlike the 2D work of Shen et al. (2011); Ye et al. (2019), structures that appear as separate plasmoids might actually be 2D projections of turbulent structures. In panel (b), a pair of termination shocks (TS) are formed above

the flare loops and under the FR with the average upstream velocity of about 1028 km/s. Particularly, the 3D interface of TS resembles a thin and long ribbon above the flare loops in our simulation. From panel (c) and (d), one can see apparent oscillations both in the x- and y-directions inside the CS and at the location of TSs from the time when blobs appear, unlike the 2D work of Takahashi et al. (2017).
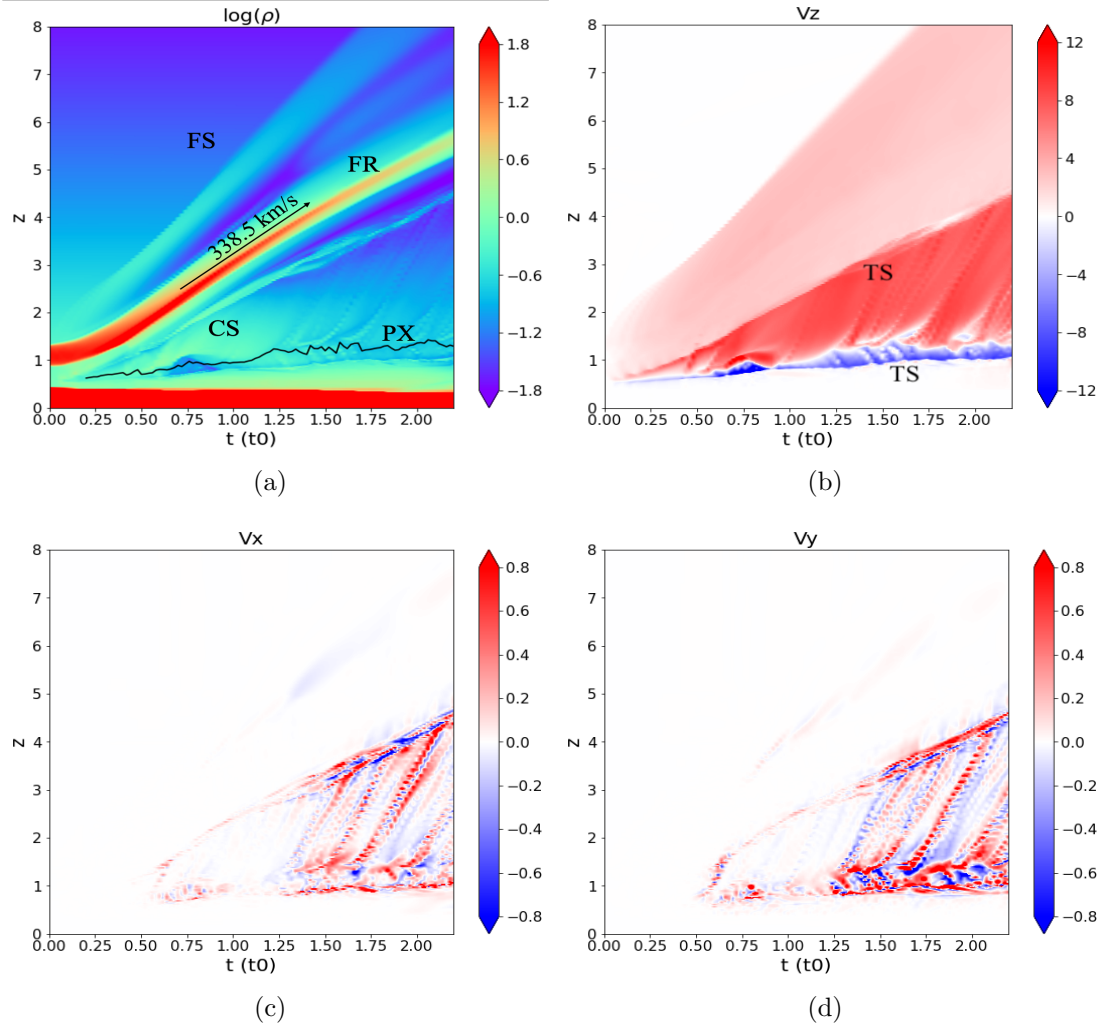

Figure 2. Time evolution of the CS along the z-axis passing the origin. (a) Mass density in log-scale; (b) velocity in the z-direction; (c) velocity in the x-direction; (d) velocity in the y-direction. The solid black line in (a) stands for the PX line.

By integrating the dimensionless energy equation over the volume V and applying the divergence theorem, we have

$$\int_V \frac{\partial}{\partial t}(\mathcal{E} + \mathcal{K} + \mathcal{W})dV = \int_V \rho \mathbf{v} \cdot \mathbf{g}dV - \int_S \left[(\frac{\gamma P}{\gamma - 1} + \frac{\rho v^2}{2})\mathbf{v} + \mathbf{E} \times \mathbf{B} + \mathbf{F}_C \right] \cdot d\mathbf{S}, \quad (15)$$

where $\mathcal{E}$, $\mathcal{K}$, $\mathcal{W}$ are the thermal, kinetic and magnetic energy densities, respectively. Note that $\mathbf{E} = \eta \mathbf{J} - \mathbf{v} \times \mathbf{B}$ is the electric field. The variations of magnetic , kinetic and thermal energies ΔE_M,

ΔE_K, ΔE_I in the entire simulation domain are given by,

$$\Delta E_M = E_M(t) - E_M(0) + \int_0^t \int_S \mathbf{E} \times \mathbf{B} \cdot d\mathbf{S}dt \tag{16}$$

$$\Delta E_K = E_K(t) - E_K(0) - \int_0^t \int_V \rho\mathbf{v} \cdot \mathbf{g}dV\,dt + \int_0^t \int_S \left(\frac{\rho v^2}{2}\right)\mathbf{v} \cdot d\mathbf{S}dt \tag{17}$$

$$\Delta E_I = E_I(t) - E_I(0) + \int_0^t \int_S \left[(\frac{\gamma P}{\gamma - 1})\mathbf{v} + \mathbf{F}_C\right] \cdot d\mathbf{S}dt \tag{18}$$

Since we are mainly interested in the energy change in the corona and want to reduce the influence from the imperfect handling of the lie-tied condition at the bottom, the above integrals are only calculated for the height $z \geq 0.5$. Figure 3 shows the time evolution of total magnetic, kinetic and thermal energy variations in the corona, calculated from the data of the AMR level 1. The magnetic energy declines gradually as magnetic reconnection proceeds. And the kinetic energy transferred from the magnetic energy dominates during the entire simulation time, and gradually accumulates and saturates. The generated thermal energy manifests in a piecewise linear phase with the steeper slope after $t \approx 0.52$, corresponding to the end of the acceleration phase. The error on the global energy diagnostic, estimated by the loss of the initial total energy $[\Delta E_M(t) + \Delta E_K(t) + \Delta E_I(t)]/[E_M(0) + E_I(0)]$, remains smaller than 4% overall. Although 5 AMR levels are utilized in our simulations, the error is computed from the data of the AMR level 1 to save the computational time. Hence, it only gives an upper limit of the numerical error, the actual error could be even smaller, indicating that the simulation runs are quite accurate to respect the energy conservation law. However, some of the total energy is lost due to numerical dissipation.
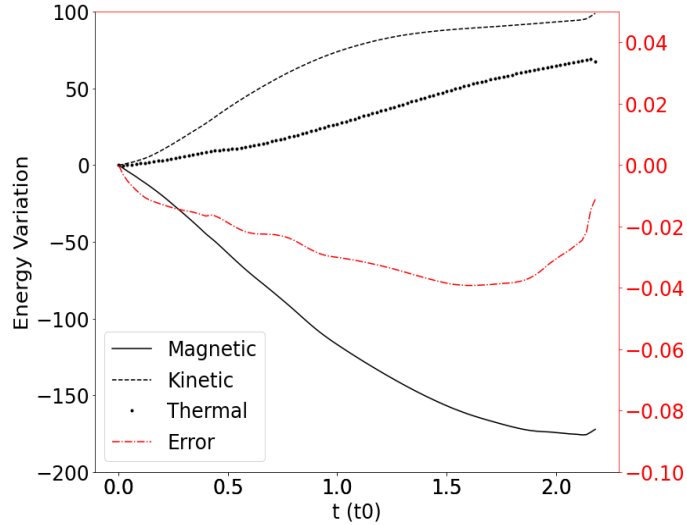

Figure 3. Time evolution of the variations in total magnetic, kinetic and thermal energies in the corona (in dimensionless units). The red dash-dotted line is the error on the total energy estimated by $[\Delta E_M(t) + \Delta E_K(t) + \Delta E_I(t)]/[E_M(0) + E_I(0)]$

Regarding the magnetic reconnection process, we calculated the reconnection rate by estimating the Alfvénic Mach number in the inflow region near the PX-line in the 3D configuration (Forbes &

Lin 2000; Jiang et al. 2021). To do so, we compute the global rate from the average inflow velocity and the Alfvén speed, and the maximum rate along the PX-line. In Figure 4(a), we present the global and maximum rates for time $t \geq 0.2$, when the sheet-like CS is well formed between the CME and the flare. As we can see, the global rate decreases in the impulsive phase (uniform stage) for $t < 0.5$ and then oscillates and decays at the same time (nonuniform stage), which is consistent with the observation work of Song et al. (2018). In the first stage, the reconnection process is externally driven by the FR motion, resulting in a large reconnection rate greater than 0.1 at the very beginning. Later in the second stage, the self-organized plasmoid or turbulent reconnection might play a competing role causing peaks in the reconnection rates. The global and maximum rates are close for $t < 0.5$, indicating that it is in the linear phase with almost the same magnitude, while they deviate from each other for $t \geq 0.5$ because of the appearance of plasmoids. In Figure 4(b), we plot also the local reconnection rate at each PX-point along the y-axis at times $t = 0.52$ and 1.42. At $t = 0.52$, the reconnection rate greatly increases between y=-0.18 and y=0.18, where the first plasmoid is just generated (See Figure 8). At $t = 1.42$, the CS becomes very turbulent with the appearance of many plasmoids, and the rate is enhanced along the PX-line by different amplitudes depending on the location of these plasmoids (See also Figure 8). In other words, every PX-point along the PX-line can have a different reconnection rate, and turbulence normally brings in a higher rate in local area for a given time.
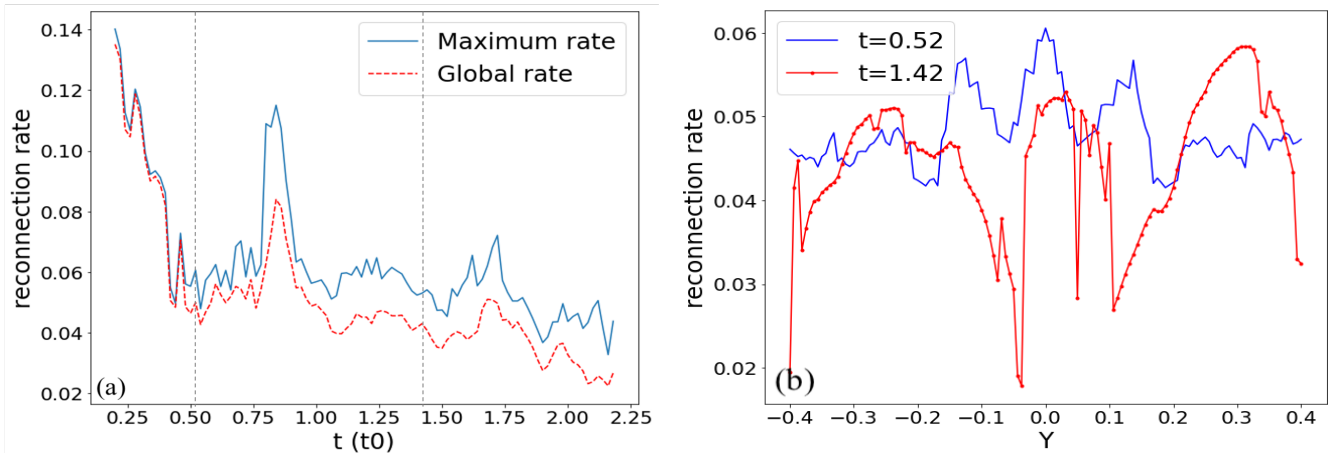

Figure 4. (a) Magnetic reconnection rates as a function of time; (b) Local reconnection rates along the y-axis at times $t = 0.52$ and 1.42. Vertical dashed lines in panel (a) mark two selected moments for plots in panel (b).

3.2. Fine structures and processes of the CS

In this section, we will focus on the small-scale fine structures in the 3D CS formed during the solar eruption. For instance, one can see that the global CS layers have already turned into the very turbulent state at $t = 1.42$ in Figure 1. At this time, we display the planar cuts of different parameters in Figure 5. Panel (a) presents the distributions of the current density, divergence and velocity curl on the vertical slice at the center ($y = 0$). The CS below the PX-point stays extremely thin due to the high pressure nearby, and the magnetic field displays a Sweet-Parker configuration. Meanwhile, the magnetic field above the PX-point forms the 'W' shape and the plasma flow presents a classical Petschek configuration with a pair of the slow-mode shocks (SSs). The existence of plasmoids thickens

the local CS width and makes the reconnection process even more complex. By following the work of Wang et al. (2009), the divergence and the curl of velocity are useful information for identifying the location of fast-mode shocks (FSs) and SSs, respectively. One can notice particularly that a pair of TSs form the valleys of the plasma at the tips of the CS, where the divergence takes the minimum value. The strong compression of the plasma occurs at the location of the TSs, and the interface of the upper TS is much larger than the lower one. Also , SSs are generated from the PX-point and propagate bi-directionally along the field lines, which can be identified from Rankine-Hugoniot relations (Shiota et al. 2005; Mei et al. 2020). Notice that the flare loop-top and the buffer region under the FR are full of the SSs, which are the important contributors to the local plasma heating. Figure 5(b) displays the horizontal slices of the current density at different heights of the CS. As we can see, the two ends of the CS in the xy-plane are connected to the arms of the FR. At the low altitudes of the CS at $z = 1.1$ and $z = 1.3$, the thickness of the CS is very thin, but it can be broadened locally by the existence of the blobs. At the high altitudes at $z = 1.8$ and $z = 2.2$, the thickness of the CS is larger and becomes very nonuniform in the y-direction. Lastly in the buffer region at $z = 3$, the CS is extremely disrupted by the turbulence, which is triggered by the Rayleigh-Taylor instability suggested by Xie et al. (2022). From lower to higher position, the fan of the CS becomes more and more tilted and forms an inverse 'S' structure for the upper CS due to the global deflection of FR during the eruption.

In order to understand how the plasma is heated in the CS, we rewrite the energy equation as:

$$\frac{\partial T}{\partial t} = -\mathbf{v} \cdot \nabla T - (\gamma - 1)T\nabla \cdot \mathbf{v} + \frac{\gamma - 1}{\rho}(-\nabla \cdot \mathbf{F}_C + \eta J^2), \tag{19}$$

where the terms $-\mathbf{v} \cdot \nabla T$ and $-(\gamma - 1)T\nabla \cdot \mathbf{v}$ are the advection and adiabatic terms, $-\nabla \cdot \mathbf{F}_C$ is the thermal conduction term, and ηJ^2 is the ohmic heating term. The density, temperature and different heating terms on the xz-plane at the center $(y = 0)$ are shown in Figure 6. Here, the calculations are based on the data of the AMR level 5, and the sampling period is $0.02t_0$. At the early time $t = 0.52$, the density and temperature distributions show a clear Y-structure above the flare loops, and the hot dense CS becomes extremely thin. The adiabatic term is primarily positive inside the CS due to compression of the plasma by the strong reconnection inflows, except for its upper end. The ohmic heating is at least two orders smaller than the adiabatic one, and conduction is a dominating contributor against the other heating terms in the CS, at the flare loop-top and around the CME bubble. At $t = 0.96$, more plasma accumulates in the upflow region to make the upper CS width larger, where the density and temperature distributions become quite smooth. The adiabatic term is only large in the lower CS and at two ends of the global CS due to the compression by TSs. The ohmic heating term is most important in the lower CS. Thermal conduction spreads the temperature out of the CS and produces a "thermal halo" around it (Seaton & Forbes 2009). This can be seen in the hot temperature structure, which is much wider than the dense region at the same location. Later at $t = 1.42$ and 1.64, the CS becomes long and thin, stretched by the rising FR, and many hot and dense plasmoids or blobs can be seen therein. At these times, the adiabatic and thermal conduction terms fragment into small pieces. From the density distribution, one can see the tuning fork structures formed above the flare loops and at bottom of the CME with two arms highly compressed, where the adiabatic and conduction effects are still significant. The ohmic term remains ignorable compared with other heating terms. We note that the conduction term is strongly concentrated in regions with high temperature gradients, indicating that the AMR resolves these

regions. For instance, the thin heating regions at $t = 0.96$ at $z = 1.5$ are resolved into 52 grid cells by AMR. As discussed in Figure 3, the total energy is lost due to numerical dissipation in terms of the viscous heating. In order to quantify the loss of energy, the numerical kinematic viscosity coefficient due to the upwinding scheme as Reeves et al. (2019) is estimated with the equation

$$\nu_N = \sum_{i,j,k} \frac{v_i \Delta x_i}{2}\left(1 - v_i \frac{\Delta t}{\Delta x_i}\right), \tag{20}$$

where Δx_i is the grid spacing for the ith dimension, i.e. $(\Delta x, \Delta y, \Delta z)$, v_i is the plasma velocity in the cell in the ith dimension, and Δt is the time step in the code. Then the excess viscous heating produced by the numerical diffusion reads as

$$H_{\text{nvisc}} = \rho \nu_N \left[\frac{1}{2}e_{ij}e_{ij} - \frac{2}{3}(\nabla \cdot \mathbf{v})^2\right], \tag{21}$$

where e_{ij} is the rate-of-strain tensor. On the other hand, we roughly measure the kinematic viscous coefficient ν_m by adding the numeric term $(\gamma - 1)H_{\text{nvisc}}/\rho$ into the right side of Eq.(19) as follows:

$$\nu_m = \frac{\left|\frac{dT}{dt} + \mathbf{v} \cdot \nabla T + (\gamma - 1)T\nabla \cdot \mathbf{v} - \frac{\gamma-1}{\rho}(-\nabla \cdot \mathbf{F}_C + \eta J^2)\right|}{(\gamma - 1)\left[\frac{1}{2}e_{ij}e_{ij} - \frac{2}{3}(\nabla \cdot \mathbf{v})^2\right]}. \tag{22}$$

For comparison, ν_N and ν_m are averaged over the region with $(x, z) \in [-0.2, 0.2] \times [0.5, 3.5]$ for $t = 1.42$ and 1.64 in Figure 6 to suppress the unnecessary errors, which both give the value close to 0.0035. This confirms that Eq.(20) is a reliable way to quantify the numerical diffusion. Figure 7 plots the density, temperature, together with the heating terms along the central line ($x = 0$) in Figure 6. The ohmic term is multiplied by 10 to be visible. Here, we also plot the numerical viscous heating. At $t = 0.52$, the density peaks at the core of the CME and the CS length is short. The temperature in the CS reaches over 20 MK and is highest at the upper end. The dT/dt is mostly negative in the CS, but it becomes positive and relatively strong near the upper end of the CS, indicating strong heating at the CME bottom. The numerical diffusion is shown to be generally greater than the ohmic term with the two peaks at the ends of the CS. The adiabatic term at this time is the main contributor for heating in the CS. Conduction is the dominating factor that cools the lower half CS and transfers the heat to the bottom of the CME. Advection plays a similar role to conduction but with the magnitude much smaller. At $t = 0.96$, the CS is stretched longer by the rising FR and the super hot structure (> 10 MK) concentrates only in the lower CS between $z = 0.8$ and $z = 1.1$. All heating terms including the numerical diffusion behave similarly as the previous time except that they are more smooth in the upper CS for $z > 1.1$. At $t = 1.42$ and 1.64, the CS enters the fragmented and fully turbulent phase due to plasmoid instability (Shen et al. 2011; Ye et al. 2019). The temperature of the CS reaches 17.5 MK and the range of temperatures is relatively narrow as observed in Warren et al. (2018). The hot and dense plasmoids or blobs start to disrupt the distributions of the density and temperature in the CS. The numerical diffusion has become significant due to the large local velocity or velocity changes produced by the instabilities in the CS, indicating a higher viscous heating rate around the plasmoids or blobs. The adiabatic term remains mostly positive in the lower half of CS due to the strong compression by the reconnection inflows. And the advection term mainly plays a role for cooling the plasma against the adiabatic

term. Thermal conduction serves to smooth out the temperature distribution along the CS, and the large magnitude of this term is mainly located in the lower half CS. It implies that substantial heat is conducted to the lower end of the CS to make the flare loops hotter rather than the CME.
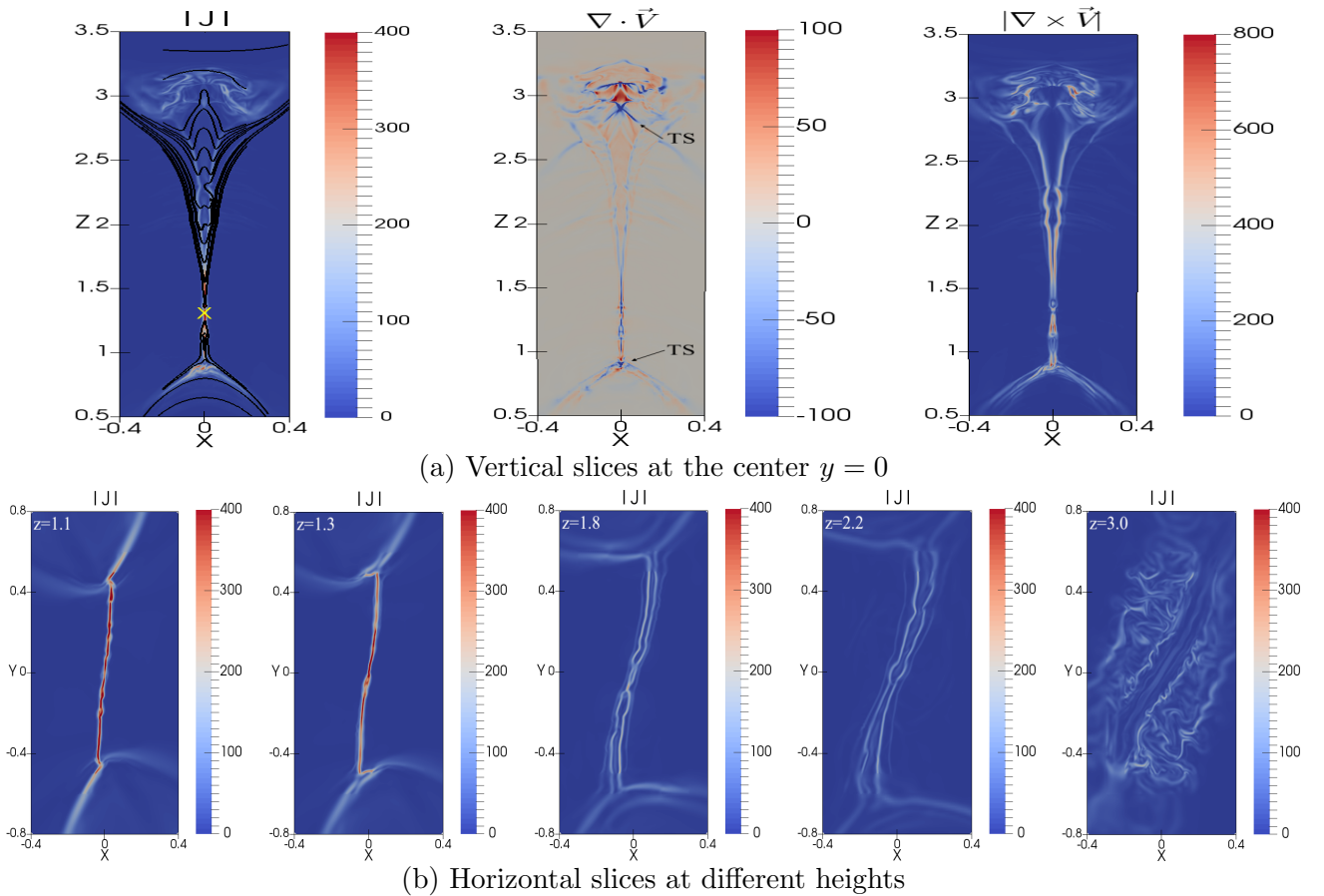

(a) Vertical slices at the center $y = 0$

(b) Horizontal slices at different heights

Figure 5. (a) Distributions of the current density $|J|$, divergence $\nabla \cdot \vec{V}$ and velocity curl $|\nabla \times \vec{V}|$ on the xz-plane at $t = 1.42$. (b) Current density on the xy-plane at different heights. The black solid lines in the current density distribution in panel (a) are the magnetic field and the yellow cross 'X' therein shows the PX-point on this slice.
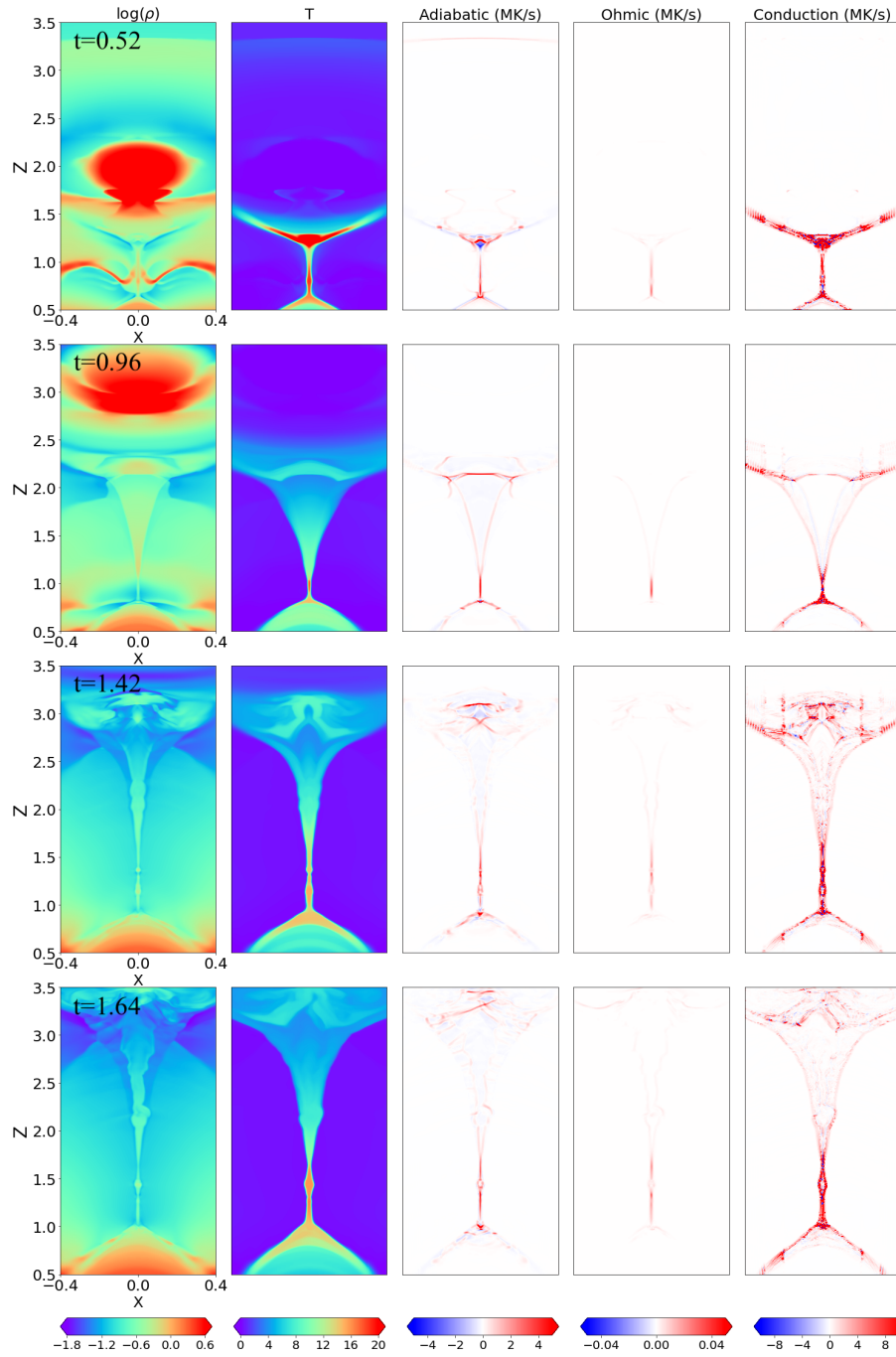
Figure 6. Log of density (first column), temperature (second column), adiabatic term (third column), ohmic heating (fourth column) and thermal conduction (fifth column) for the xz-plane at the center ($y = 0$) at different times. Note that the contribution from adiabatic, ohmic heating and thermal conduction is shown in cgs units for better understanding the plasma heating process in the current sheet.
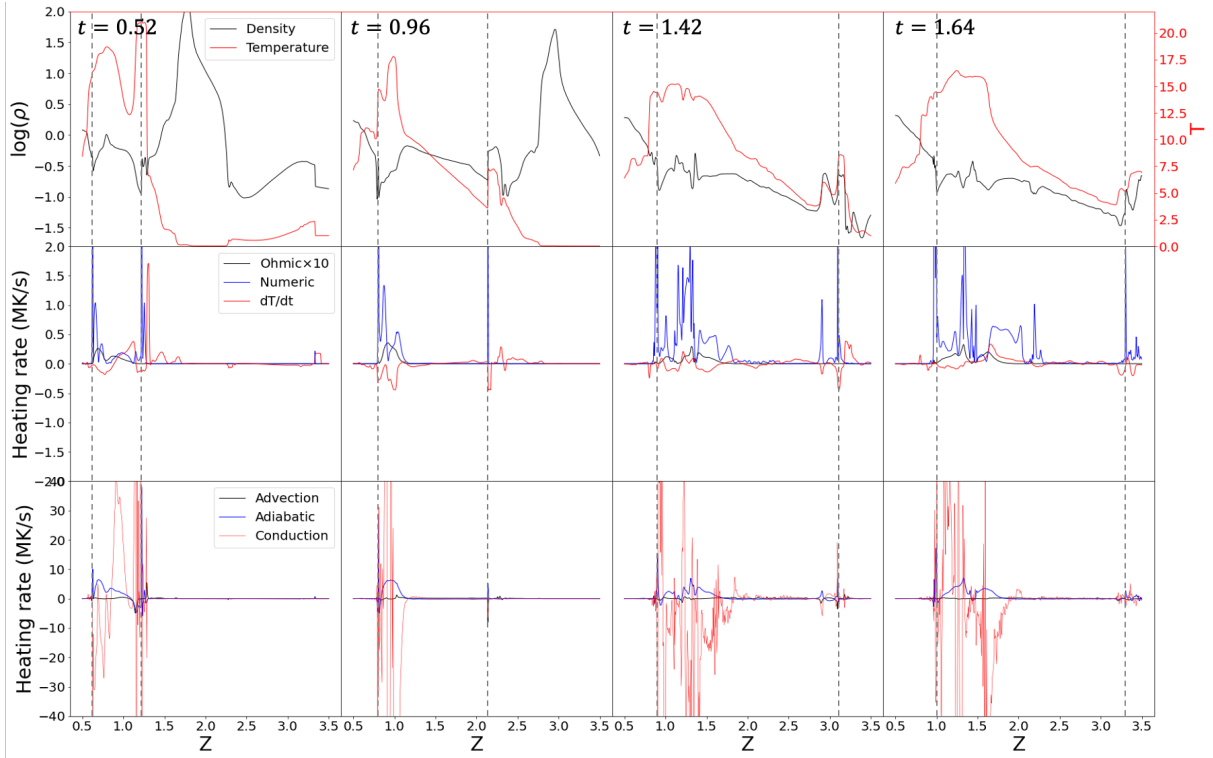
Figure 7. Plots of quantities along the central line (x=0) in Figure 6 at the same times as in this figure: density and temperature (first row), heating terms and change in the temperature (dT/dt) and heat transport terms. The vertical dashed lines mark the current sheet ends.

We present the face-on view of the region of interest including the flare and a part of CS at the center plane (x=0) for selected times in Figure 8. The physical quantities shown are averaged along the line of sight (LOS) for the length of $x \in [-0.1, 0.1]$. For the early stage of the eruption at $t = 0.52$, the first plasmoid just appears and the reconnection outflows are closely uniform. The y- and z-direction velocity fields oscillate slightly in the region under the FR rather than the loop-top region. The flare structure in the synthetic AIA $131\mathring{A}$ map is smooth, while the CS shows a cavity inside due to the low density region formed by the reconnection inflows. Later at $t = 0.96$, the current distribution at the flare loop-top becomes turbulent, where oppositely directed plasma outflows appear. Unlike the 2D cases (Ye et al. 2019, 2020), the reconnection outflows in 3D are not only along the flare arcades in the xz-plane, but also have the apparent movement in y-direction. The mixture of negative and positive velocities in the y- and z-directions at the interface region of the strong electric current indicates that turbulent reconnection may readily occur. Accordingly in the channel of AIA $131\mathring{A}$, the finger-like structures, known as SADs, can be observed between the post-flare loops and the loop-top, which are formed due to the Rayleigh-Taylor or Richtmyer-Meshkov instabilities (Shen et al. 2022). Then at $t = 1.42$, the reconnection engages into the nonlinear phase with highly nonuniform velocity field in the CS. One can easily recognize the blobs in different flux tube substructures from the current distribution in the CS, and the velocity distribution of each blob can be also different. If one blob particularly has both negative and positive values of V_z, the splitting process occurs, which cannot be seen in 2D cases (Ye et al. 2019; Zhang et al. 2022). In the AIA $131\mathring{A}$ image, the height of SADs increases with the accumulated flare arcade, and the moving blobs are slightly brighter than the

background CS fan, which might extend the spikes of SADs to a higher place above the loop-top. From the first column of this figure, one can see that the PX position is never at the same height along the y-axis, especially that the complex structures of blobs can strongly disrupt the primary reconnection sites.

Furthermore, we study the turbulence amplitudes in space by estimating the turbulent kinetic and magnetic energy densities at different times. The velocity and magnetic fluctuations δV and δB are defined as, respectively,

$$
\begin{aligned}
\delta V(t,x,y,z)^2 = {} & (V_x(t,x,y,z) - \langle V_x \rangle (t,x,z))^2 \\
& + (V_y(t,x,y,z) - \langle V_y \rangle (t,x,z))^2 \\
& + (V_z(t,x,y,z) - \langle V_z \rangle (t,x,z))^2,
\end{aligned}
\tag{23}
$$

and

$$
\delta B^2 = (B_x - \langle B_x \rangle)^2 + (B_y - \langle B_y \rangle)^2 + (B_z - \langle B_z \rangle)^2,
\tag{24}
$$

where $\langle \cdot \rangle$ is taken as the average value in the y-direction for the region of interest. Particularly, we choose here to compute the average value for a physical quantity over the length for $y \in [-0.2, 0.2]$. Then the turbulent kinetic energy density is given by $< \rho > < \delta V >^2 /2$, and the turbulent magnetic energy density is $< \delta B >^2 /2$. Figure 9 shows the spatial distributions of the corresponding turbulent energy densities at different times. At $t = 0.96$, the turbulent component of kinetic energy generally dominates over that of magnetic energy in the CS except the region very close to the PX-line (see Figure 8). Then the turbulent kinetic energy density becomes smaller and breaks up into small pieces at $t = 1.42$ and 1.64. At these times, the turbulent components of kinetic and magnetic energies are comparable, and their distributions with height are highly inhomogeneous. We notice that both energy densities somewhat enhanced at the loop-top region, resulting from the interchange instabilities of backflows therein (Takasao & Shibata 2016). And the turbulence of kinetic energy is shown to be the strongest at the loop-top, which is consistent with the observational work of Kontar et al. (2017); Stores et al. (2021).
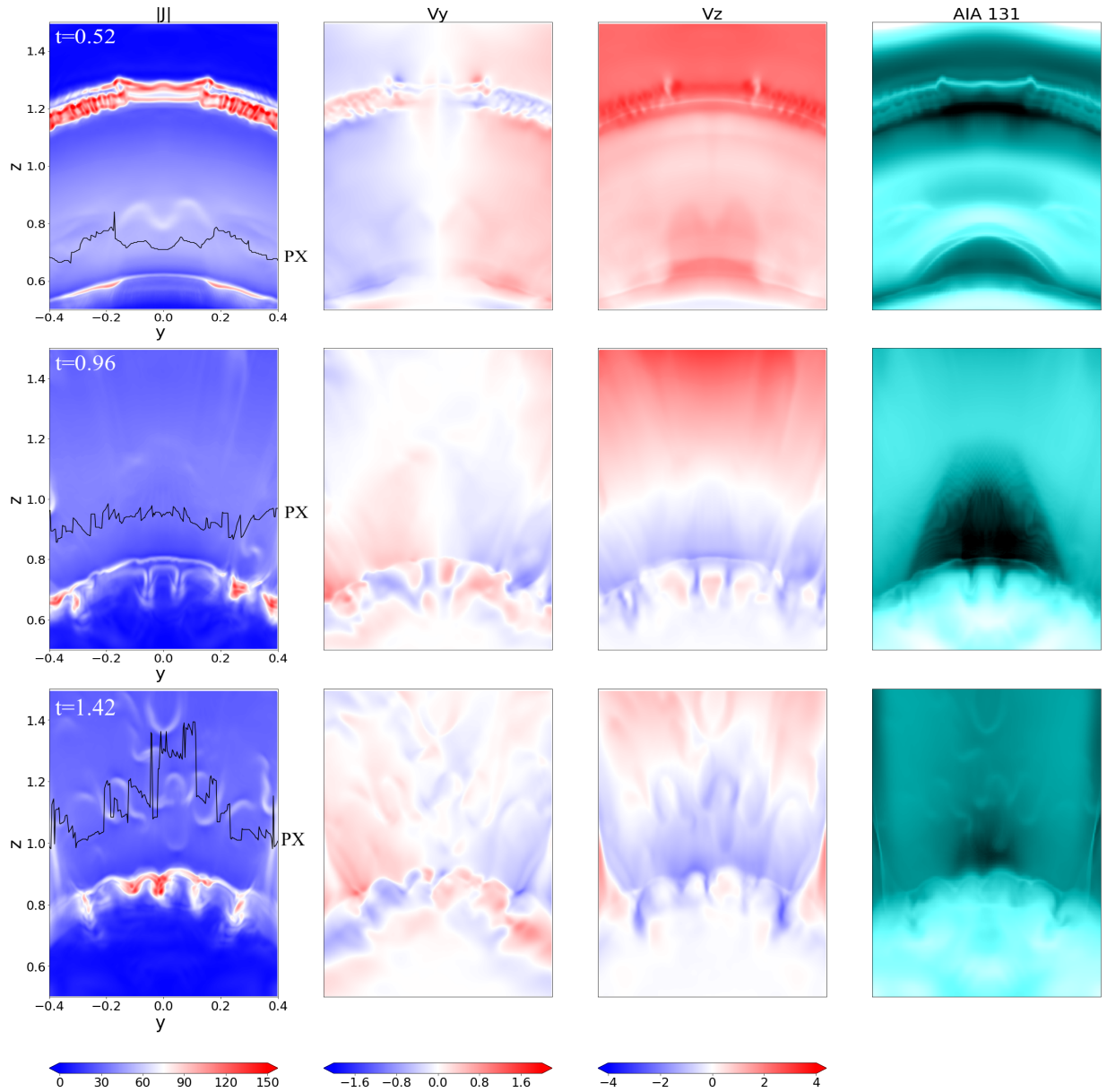
Figure 8. Face-on view of the CME-flare current sheet at given times $t = 0.52, 0.96, 1.42$. From left to right for each row, there are the current density $|J|$, velocities V_y, V_z in the y- and z-directions, and synthetic EUV image for AIA 131 $\mathring{A}$. The black solid lines in the first column are the PX-lines. Note that $|J|, V_y, V_z$ are averaged over the LOS for $x \in [-0.1, 0.1]$.
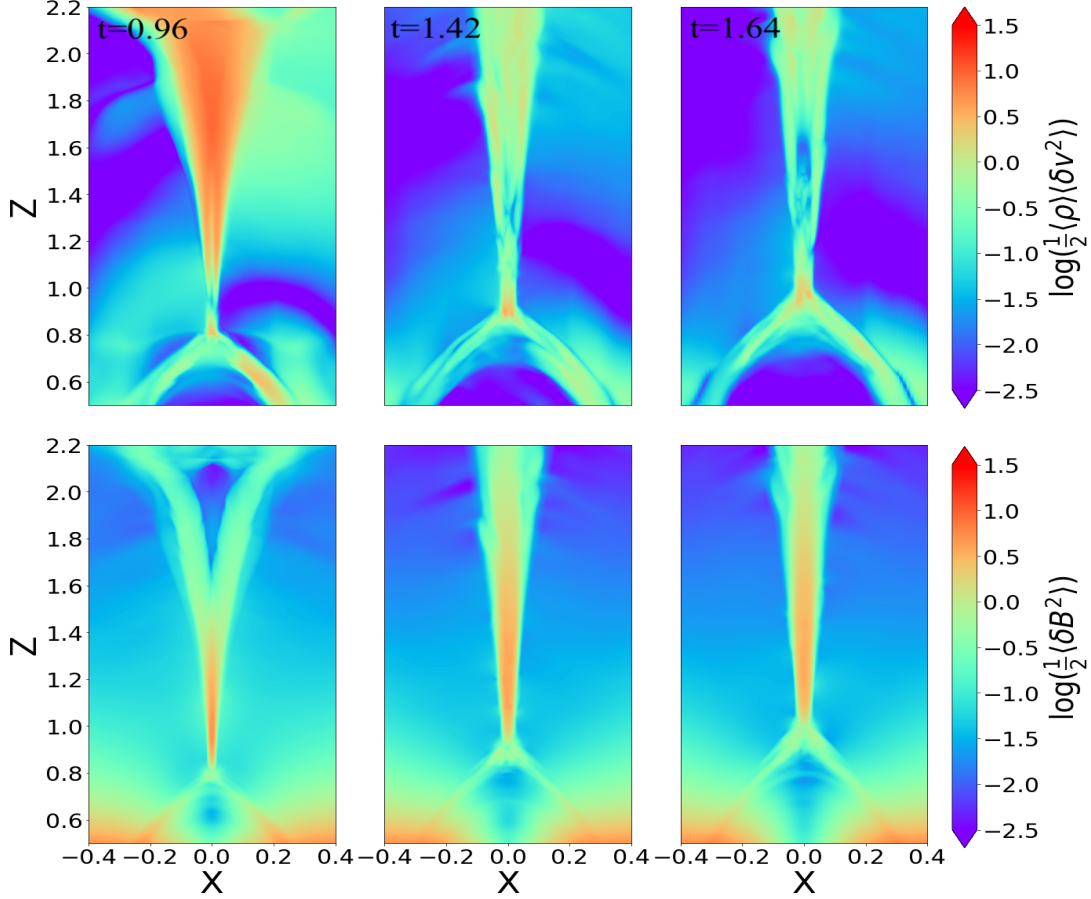
Figure 9. Distributions of the turbulent kinetic and magnetic energy density at different evolution times $t = 0.96$, 1.42 and 1.64.

Additionally, it is worthwhile to quantify the anisotropy of turbulence at different heights of the CS. By picking up the simulation data at $t = 1.42$ (see Figure 1), we select four cubic boxes A-D in four specific regions: in the flare loops, close to the PX, far above the PX and under the CME. The boxes are defined as A: $[-0.2, 0.2] \times [-0.2, 0.2] \times [0.6, 1]$, B: $[-0.2, 0.2] \times [-0.2, 0.2] \times [1, 1.4]$, C: $[-0.2, 0.2] \times [-0.2, 0.2] \times [1.8, 2.2]$ and D: $[-0.2, 0.2] \times [-0.2, 0.2] \times [2.8, 3.2]$ in (x, y, z) coordinates. Figure 10 shows the average Fourier power spectra obtained from the velocity field for each box as a function of the wavenumber k, normalized by the characteristic length L. The power spectra are calculated using 3D Fourier transform (Kirby 2005) and then the spectrum in each direction is obtained by summing up the power coefficients in the other directions. The associated Fourier transforms show kinetic structures in the x-, y- and z-directions, respectively. In box A, B and C, the power in the y- and z-directions show reasonable power law behavior from 100 or $200L^{-1}$ to 700 or $800L^{-1}$. The slopes are flatter than the dotted lines associated with the x-direction. The power in the x-direction seems to be curved rather than power law, or to consist of several narrow power law intervals. Box B pertains to the X-line region where turbulence is strongly driven. It is complicated by the fact that the CS is narrower than the box, so x-direction power at small k is suppressed. So the x-direction might not have a clear inertial range, but there is an excess of power on scales of the roughly CS thickness, which varies with the height z. Box D clearly shows well-developed, isotropic

turbulence. In this case the slopes in the power law portions at small scales seem to agree with the range -1.5 to -1.7 expected for Goldreich-Sridhar or Kolmogorov turbulence (Beresnyak 2017). That turbulence is probably driven by the interaction between the reconnection outflow and the erupted flux rope, as described in Ye et al. (2021). That could account for the higher overall level of power at all scales. There has been considerable work on the power law indices and the inner and outer scales of turbulence in simulations of current sheets (Bárta et al. 2011; Shen et al. 2013; Boldyrev 2006; Boldyrev & Loureiro 2020; Kowal et al. 2017; Edmondson & Lynch 2017; Zharkova & Xia 2021; Ye et al. 2019, 2020). Given the limited inertial range and the gradual character of the change in slope at large wavelengths in our simulations, there is some uncertainty in both the spectral index and the outer scale.

If the x-direction turbulence in box C has evolved from that in box B, the higher power at large scales could be partly due to the larger CS thickness far from the X-point. The smaller power at small scales could result from mergers of islands. It seems too steep to result from cascade to the dissipation scale. In box A in the flare loops, one could also imagine that the stronger power at large scales comes about because the CS is thicker. There may be an inertial range with a somewhat steeper slope than the y- and z-directions. The TS will strongly affect the turbulence, as in Shen et al. (2018), but the spectra are similar enough to the spectra near the X-line that they may be strongly influenced by the turbulence advected from above.
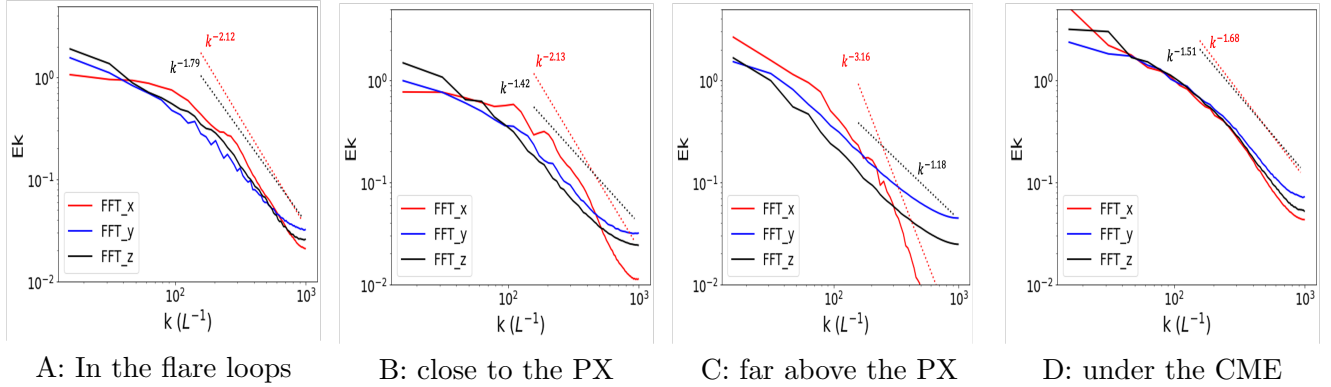

A: In the flare loops   B: close to the PX   C: far above the PX   D: under the CME

Figure 10. Fourier power spectra of the velocity in the $x-$, $y-$ and $z-$directions for different parts of the CS as a function of the wavenumber k. The red and black dotted lines in each panel denotes the spectral slopes in the x- and z-directions for different regions.

Lazarian et al. (2020) suggest that turbulent reconnection process dominates in 3D CS layers. However, the reconnection mechanisms proceeding in a CME-driven CS remain unclear. We follow the evolution of the downward blobs for four successive times just after the generation shown by Figure 11. In panel (a)-(d), the tube-like blobs marked by the black box are generated and move downward to interact with the flare loop-top. At $t = 1.38$ in panel (e), two separate plasmoids are generated and recognized by unenclosed and highly twisted magnetic field lines. By plotting the field lines in different colors, we can observe the magnetic structures of blobs more clearly. Then at $t = 1.40$ in panel (f), they begin to merge into a bigger plasmoid by changing the connectivity of the field lines, i.e. magnetic reconnection. This process of plasmoid coalescence is totally different from that in 2D, which yields a transverse (horizontal) CS of opposite current density between the mergers (Bárta et al. 2011). The kinking of the plasmoid can also happen in the middle by obtaining

extra twist turns. At $t = 1.42$, the big plasmoid starts to collide with the flare loop-top, and is split into two separate plasmoids. The lower plasmoid loses its twist consecutively at one end during the collision, and the annihilation process of the plasmoid is likely to be related to turbulent reconnection occurring at the loop-top region. Lastly at $t = 1.44$, the rest of the lower plasmoid also falls to the flare loops with two ends attached to the loop-top. The 3D complex structures and processes of plasmoids naturally provide multiple reconnection sites when merging into the flare loops.

On the other hand, we show the evolution of a blob moving upwards from $t = 1.56$ to $t = 1.64$ in Figure 12. In panel (a)-(c), a blob of 'U' shape leaves the PX-line with a speed of about 1285 km/s and becomes eventually messed up far away from the PX-line in a short time. Regarding the field lines in panel (d), the blob is highly twisted in the center at $t = 1.56$, which can be identified as a plasmoid. Then at $t = 1.60$ in panel (e), the plasmoid swells while rising due to the low gas pressure at higher altitudes, and the turns of the flux tube are reduced. Later at $t = 1.64$ in panel (f), the plasmoid only has 2 turns left at its two sides, and evolves gradually into a set of magnetic lines in a 'W' shape accompanied by SSs in various directions. This is to say, upward plasmoids are generated due to tearing instabilities, and evolve into the stochastic meandering of magnetic field lines (i.e. turbulence) in a short time, which induces a strong violation of magnetic flux freezing and a rapid energy dissipation (Eyink et al. 2013). Hence, the blob-like structures often observed in the flare CS (Lin et al. 2005; Cheng et al. 2018) are not necessarily plasmoids, but instead turbulent post-plasmoid structures, because they were either well-developed plasmoids or merging/tearing magnetic islands. Their properties could be much different from other turbulence (e.g., around the PX region). Some of the blob-like structures seen in the flare CS have much different ionization states than the rest of the CS, for instance the ones seen in C III and O VI lines in the work of Ciaravella & Raymond (2008). Those probably are separate plasmoids. However, the ones seen in white light could be either plasmoids or turbulent features.
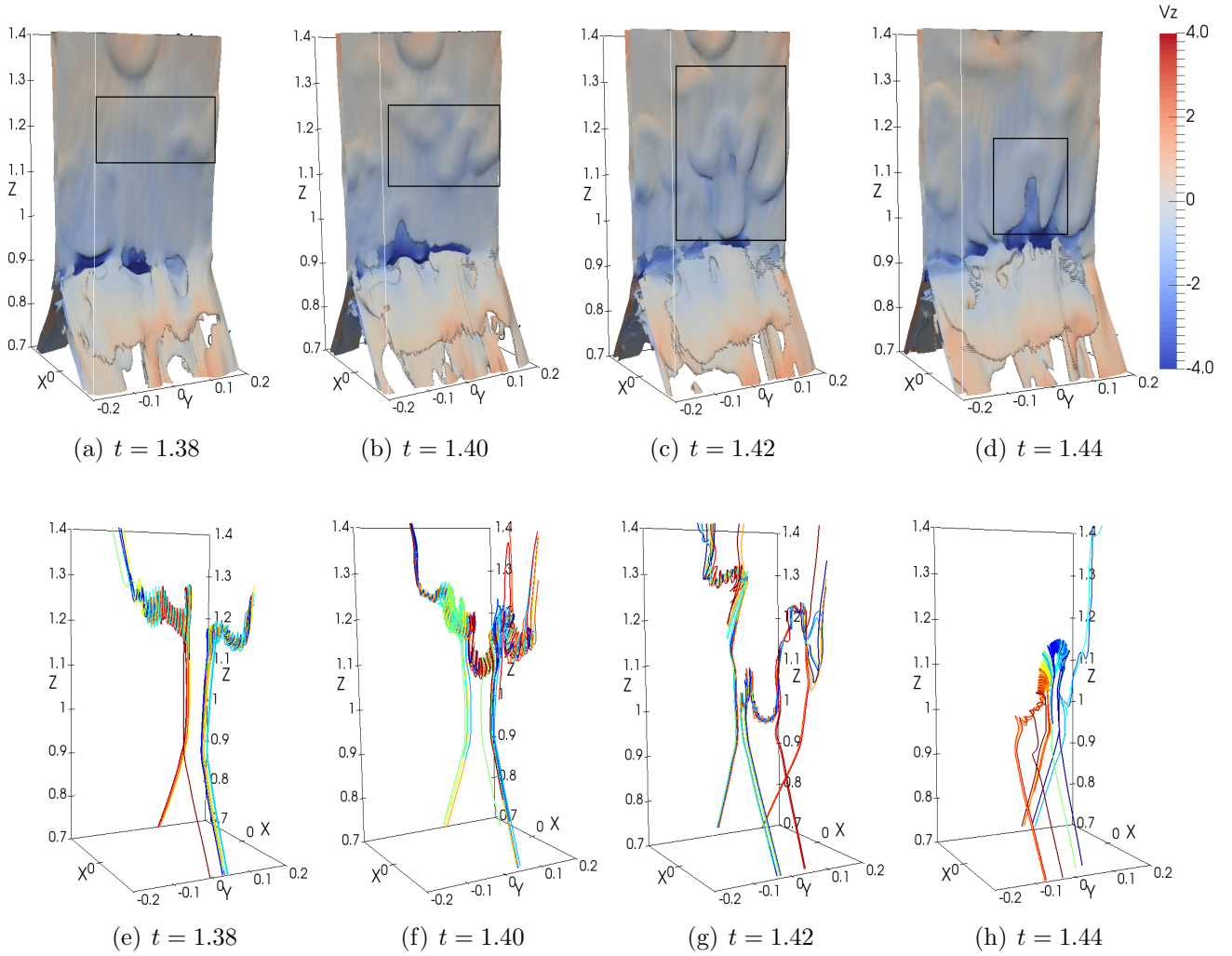
(a) $t = 1.38$ (b) $t = 1.40$ (c) $t = 1.42$ (d) $t = 1.44$

(e) $t = 1.38$ (f) $t = 1.40$ (g) $t = 1.42$ (h) $t = 1.44$

Figure 11. Detailed evolution of the downward blobs from $t = 1.38$ to $t = 1.44$. (a)-(d) Structures of the blobs shown by the current isosurface with value $|J| = 50$ colored by the velocity along the z-direction V_z at the successive times. (e)-(h) 3D magnetic structures of the blob. Note that the colors for the magnetic field lines are used to better display the different lines.
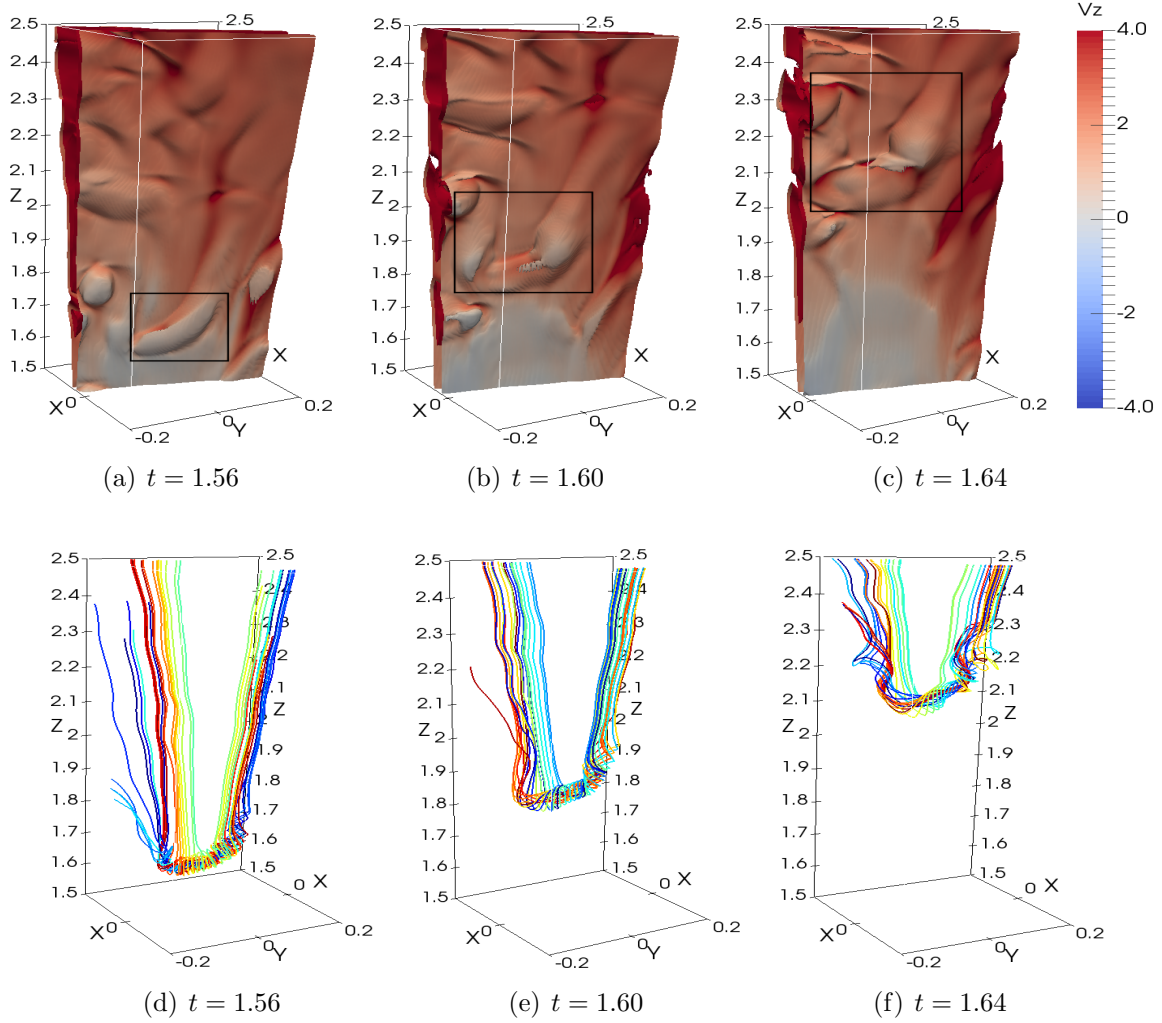
(a) $t = 1.56$ (b) $t = 1.60$ (c) $t = 1.64$

(d) $t = 1.56$ (e) $t = 1.60$ (f) $t = 1.64$

Figure 12. Detailed evolution of an anti-sunward blob from $t = 1.56$ to $t = 1.64$. The physical terms are the same as Figure 11.

As discussed by Jiang et al. (2021), the turbulent structures of CS layers become more complex in higher resolution computations. When the CME system evolves into a sufficiently turbulent stage, magnetic reconnection in the CS proceeds in a more complicated way rather than only Sweet-Parker or Petschek type. From our simulations, the downward plasmoids can keep the twisted shape until the annihilation at the flare loop-top, while many upward plasmoids turn into the turbulent post-plasmoid structures before arriving at the bottom of the FR. We can thus infer that turbulent reconnection dominates in the upper CS in 3D while plasmoid reconnection only dominates in the lower CS.

4. CONCLUSION AND DISCUSSION

Plasmoid reconnection plays a governing role in the 2D magnetized plasma, and the dissipation scale, spectral properties and energy conversion process in the large-scale CS are exhaustively studied by theoretical and numerical work (Lin et al. 2007; Shen et al. 2011; Ye et al. 2019, 2020; Zhang et al. 2022). In the realistic 3D plate-like CS formed in a solar eruption (Lin et al. 2002), the CS is highly confined by the reconnection inflows, so is the turbulence inside. However, the evolution

of the confined turbulence in the CME-flare CS remains rarely reported in 3D. Aiming on this, we have performed full 3D MHD simulations for a moderate CME based on the analytical solution of Titov & Démoulin (1999) in the gravitationally stratified atmosphere. More details are revisited and reported in the 3D view as follows:

(1) Two runs with and without thermal conduction successfully reproduce the erupted FR with the propagation speed over 300 km/s. The magnetic energy of the initial system converts into the kinetic and thermal energies, between which the kinetic energy dominates in the entire simulation time.

(2) A plane-like CS above the flare develops and deflects following the FR motion. Many blobs in different shapes are generated in the CS due to tearing and plasmoid instabilities, and they undergo the splitting, merging and kinking processes in a more complex way than 2D cases. The plasma in the CS is mainly heated by the adiabatic and numerical viscous terms, and thermal conduction is the dominant factor that balances the energy inside the CS. Accordingly, the temperature of the CS reaches about 20 MK, and the range of temperatures is relatively narrow.

(3) The reconnection rate decreases from a value larger than 0.1 in the impulsive phase, then oscillates and decays at the same time, which is consistent with the 2011 December 25 CME observed by Song et al. (2018). And the generation of plasmoids in the CS gives rise to a higher reconnection rate in local area and the local rates along the PX-line are enhanced by turbulence with different amplitudes depending on the location of plasmoids.

(4) The reconnection outflows are highly nonuniform in the 3D CS as turbulence develops, which strongly disrupt the height of the PX-line. From the face-on view, the finger-like structures of SADs can be seen above the post-flare loops in AIA 131$\mathring{A}$, which confirm the main results of Shen et al. (2022) in a more self-consistent way. Moreover, the blobs are slightly brighter than the background CS fan in AIA 131$\mathring{A}$, which might extend the spikes of SADs to a higher place above the loop-top. It means that the moving blobs can also be a part of SADs.

(5) To analyze spatially the turbulent features of the CS, the 3D Fourier transform is performed on the velocity fields at $t = 1.42$. The width and elongation of the CS might vary with height, showing the complex geometry of the 3D CS and turbulence. The spectra surprisingly have a significant variation either at different heights of the CS or in different directions, given the limited inertial range.

(6) The PX-line is located always close to the flare loops and separates the CS into two parts, causing the energy partition to be asymmetric. The annihilation processes of plasmoids are different in two bi-directional reconnection outflows. Indeed, the upward plasmoids turn into stochastic magnetic field lines in a short time after the generation, while the downward plasmoids keep the twisted field lines until their disappearance at the flare loop-top. So the sunward blob-like structures are definitely plasmoids, while the anti-sunward ones often found in observations (Lin et al. 2005; Cheng et al. 2018) are not necessarily identified as plasmoids, but instead turbulent post-plasmoid structures. That is to say, as the CS develops long enough, the plasmoid reconnection dominates in the lower CS, and the turbulent reconnection dominates in the upper CS.

In the work of Kowal et al. (2020); Lazarian et al. (2020), they reported that the plasmoid instability is only important for the initial stage of reconnection in presence of 3D homogeneous turbulence. But in our numerical work, various reconnection processes proceed simultaneously during the eruption process, in which plasmoid reconnection plays a key role for the lower CS. However, a precise calculation of the spectral slopes with respect to turbulence is still lacking due to the limited resolution in local place. A 3D high-resolution simulation of sufficiently large Lundquist number ($S = 10^5 - 10^6$) for a solar flare will be performed in the future to determine the dissipation scale and CS thickness .

ACKNOWLEDGMENTS

APPENDIX

EFFECT OF THERMAL CONDUCTION

This section is devoted to comparing the models without and with thermal conduction accomplished by our 3D MHD simulations, namely Run A and Run B listed in table 1. In Run B, the energy equation is solved with the parallel and perpendicular heat conduction formalized by

$$\mathbf{F}_C = -\kappa_{||}(\nabla T \cdot \hat{\mathbf{B}})\hat{\mathbf{B}} - \kappa_\perp(\nabla T - (\nabla T \cdot \hat{\mathbf{B}})\hat{\mathbf{B}}), \tag{1}$$

where $\kappa_{||} = 8 \times 10^{-7} \frac{T_0^{7/2}}{\rho_0 L_0 v_A^3} T^{5/2}$ and $\kappa_\perp = 4 \times 10^{-10} \frac{n_0^2}{B_0^2 T_0^3} \frac{\rho^2}{B^2 T^3} \kappa_{||}$. The heat flux can saturate when temperature gradients become extremely steep, and is limited by the saturated flux suggested by Cowie & McKee (1977):

$$\mathbf{F}_{C,\mathrm{sat}} = 5\phi\rho c_{\mathrm{iso}}^3, \tag{2}$$

where c_{iso} is the isothermal sound speed, and $\phi = 1.1$ for the fully ionized gas.

Figure 13 plots the density, temperature and current normal to plane for the xz-plane at the center ($y = 0$) at $t = 1.58$ for different runs. At this time, the CSs for Run A and B have already developed thin and long enough to let the instabilities take place. Blobs can be seen from the current density for both Runs, in which Run B shows less symmetry than the other. The density inside the CS and blobs is even lower than the background for Run A, while the CS and blobs are denser places for

Run B. The temperature along the CS ranges between 3.6 and 17 MK for Run B, and the super hot structures (> 10 MK) are mainly in the region above the flare loops. For Run A, the maximum temperature reaches 200 MK along the CS, and all the flare loops have the temperature exceeding 20 MK. As a result, thermal conduction is important to balance the energy inside the CS and yields the more realistic density and temperature distributions to compare with the observations. Together with Figure 6 and 7, thermal conduction is shown to be a dominating factor for the heat transport when the plasma is heated in the solar eruption.
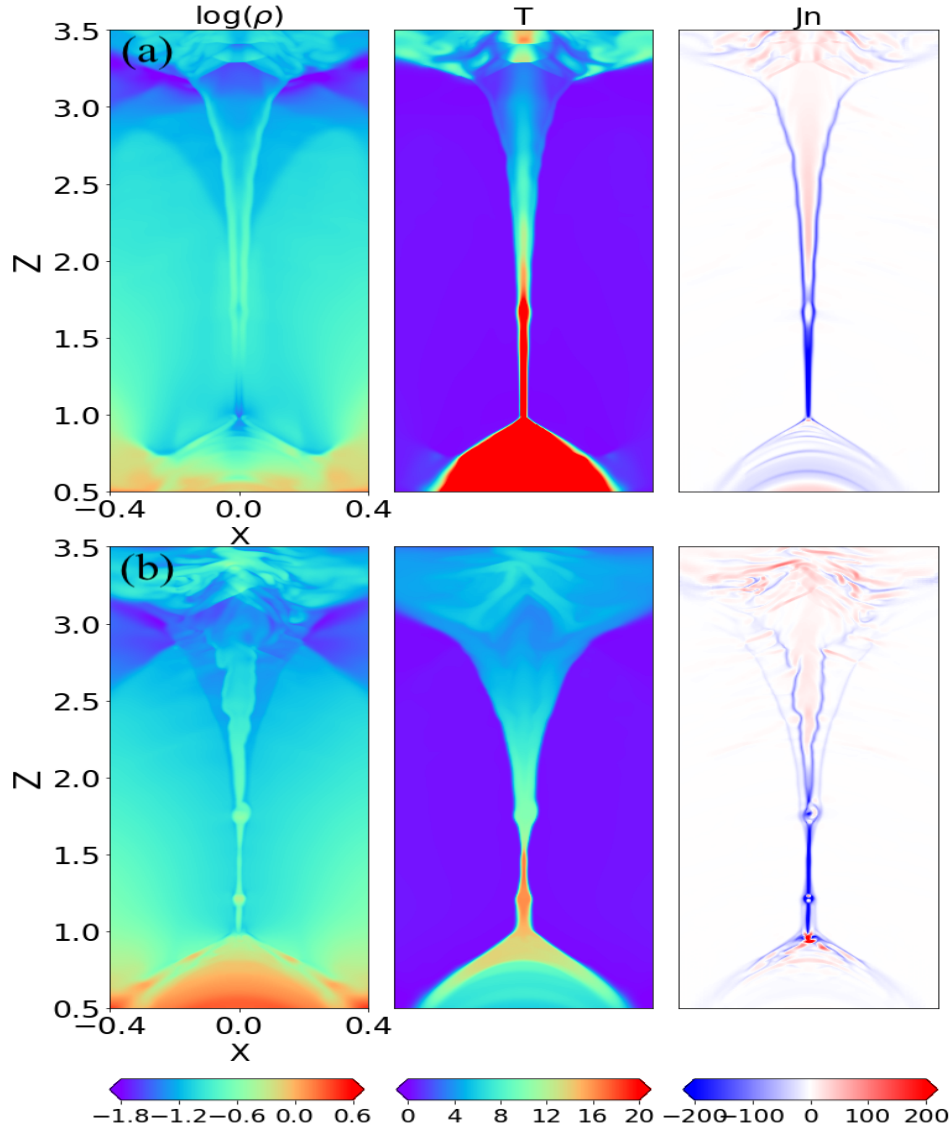

Figure 13. Log of density (first column), temperature (second column) and current normal to plane for the xz-plane at the center ($y = 0$) at $t = 1.58$. (a) Run A; (b) Run B.

Software: MPI-AMRVAC

REFERENCES

Amari, T., Luciani, J. F., Aly, J. J., Mikic, Z., & Linker, J. 2003, ApJ, 585, 1073

Antiochos, S. K., DeVore, C. R., & Klimchuk, J. A. 1999, ApJ, 510, 485

Archontis, V., Moreno-Insertis, F., Galsgaard, K., Hood, A., & O'Shea, E. 2004, A&A, 426, 1047

Bárta, M., Büchner, J., Karlický, M., & Skála, J. 2011, ApJ, 737, 24

Beresnyak, A. 2017, ApJ, 834, 47

Bhattacharjee, A., Huang, Y. M., & Rogers, B. 2009, Phys. Plasmas, 16, 112102

Boldyrev, S. 2006, PhRvL, 96, 115002

Boldyrev, S., & Loureiro, N. F. 2020, Journal of Geophysical Research (Space Physics), 125, e28185

Cai, Q., Feng, H., Ye, J., & Shen, C. 2021, ApJ, 912, 79

Cai, Q., Shen, C., Raymond, J., et al. 2019, MNRAS, 489, 3183

Cheng, X., Li, Y., Wan, L. F., et al. 2018, ApJ, 866, 64

Ciaravella, A., & Raymond, J. C. 2008, ApJ, 686, 1372

Cowie, L. L., & McKee, C. F. 1977, ApJ, 211, 135

Del Zanna, G., Dere, K. P., Young, P. R., Landi, E., & Mason, H. E. 2015, A&A, 582, A56

Dong, C., Wang, L., Huang, Y.-M., et al. 2022, Science Advances, 8, eabn7627, doi: 10.1126/sciadv.abn7627

Edmondson, J. K., & Lynch, B. J. 2017, ApJ, 849, 28

Eyink, G., Lazarian, A., & Vishniac, E. T. 2011, ApJ, 743, 51

Eyink, G., Vishniac, E., Lalescu, C., et al. 2013, Nature, 497, 466

Fermo, R. L., Drake, J. F., & Swisdak, M. 2010, Physics of Plasmas, 17, 010702, doi: 10.1063/1.3286437

Forbes, T. G., & Lin, J. 2000, Journal of Atmospheric and Solar-Terrestrial Physics, 62, 1499

Furth, H. P., Killeen, J., & Rosenbluth, M. N. 1963, Physics of Fluids, 6, 459

Hanneman, W. J., & Reeves, K. K. 2014, ApJ, 786, 95

Harten, A. 1983, J. Comput. Phys., 49, 357

Innes, D. E., Guo, L. J., Bhattacharjee, A., Huang, Y. M., & Schmit, D. 2014, ApJ, 796, 27

Isenberg, P. A., Forbes, T. G., & Demoulin, P. 1993, ApJ, 417, 358

Jiang, C., Feng, X., Liu, R., et al. 2021, Nature Astronomy, 5, 1126

Keppens, R., Meliani, Z., van Marle, A. J., et al. 2012, J. Comput. Phys., 231, 718

Kirby, J. F. 2005, Computers & Geosciences, 31, 846

Kontar, E. P., Perez, J. E., Harra, L. K., et al. 2017, PhRvL, 118, 155101

Koren, B. 1993, A robust upwind discretization method for advection, diffusion and source terms (Amsterdam: Vieweg)

Kowal, G., Falceta-Gonçalves, D. A., Lazarian, A., & Vishniac, E. T. 2017, ApJ, 838, 91

—. 2020, ApJ, 892, 50

Kowal, G., Lazarian, A., Vishniac, E. T., & Otmianowska-Mazur, K. 2009, ApJ, 700, 63

Lazarian, A., Eyink, G. L., Jafari, A., et al. 2020, Phys. Plasmas, 27, 012305

Lazarian, A., & Vishniac, E. T. 1999, ApJ, 517, 700

Lazarian, A., Vlahos, L., Kowal, G., et al. 2012, SSRv, 173, 557, doi: 10.1007/s11214-012-9936-7

Lee, J.-O., Cho, K.-S., Lee, K.-S., et al. 2020, ApJ, 892, 129

Li, Y., Xue, J. C., Ding, M. D., et al. 2018, ApJL, 853, L15

Lin, J. 2002, ChJA&A, 2, 539

Lin, J., & Forbes, T. G. 2000, J. Geophys. Res., 105, 2375

Lin, J., Forbes, T. G., & Isenberg, P. A. 2001, J. Geophys. Res., 106, 25053

Lin, J., Forbes, T. G., Ko, Y.-K., Raymond, J. C., & Vourlidas, A. 2007, ApJ, 658, L123

Lin, J., Ko, Y.-K., Sui, L., et al. 2005, ApJ, 622, 1251

Lin, J., Murphy, N. A., Shen, C., et al. 2015, SSRv, 194, 237

Lin, J., van Ballegooijen, A. A., & Forbes, T. G. 2002, Journal of Geophysical Research (Space Physics), 107, 1438

Liu, R. 2013, MNRAS, 434, 1309

Loureiro, N. F., Schekochihin, A. A., & Cowley, S. C. 2007, Phys. Plasmas, 14, 100703

Mackay, D. H., & van Ballegooijen, A. A. 2009, SoPh, 260, 321

MacNeice, P., Antiochos, S. K., Phillips, A., et al.
    2004, ApJ, 614, 1028

Mei, Z., Keppens, R., Cai, Q., et al. 2020,
    MNRAS, 493, 4816

Mei, Z. X., Keppens, R., Roussev, I. I., & Lin, J.
    2017, A&A, 604, L7

Mei, Z. X., Keppens, R., Roussev, I. I., & Lin, J.
    2018, A&A, 609, A2

Meyer, C. D., Balsara, D. S., & Aslam, T. D.
    2012, MNRAS, 422, 2102

Mikic, Z., & Linker, J. A. 1994, ApJ, 430, 898

Moore, R. L., Sterling, A. C., Hudson, H. S., &
    Lemen, J. R. 2001, ApJ, 552, 833

Nishida, K., Nishizuka, N., & Shibata, K. 2013,
    ApJL, 775, L39

Parker, E. N. 1957, Journal of Geophysical
    Research (1896-1977), 62, 509,
    doi: https://doi.org/10.1029/JZ062i004p00509

Patel, R., Pant, V., Chandrashekhar, K., &
    Banerjee, D. 2020, A&A, 644, A158

Petschek, H. E. 1964, NASA Special Publication,
    50, 425

Reeves, K. K., Freed, M. S., McKenzie, D. E., &
    Savage, S. L. 2017, ApJ, 836, 55,
    doi: 10.3847/1538-4357/836/1/55

Reeves, K. K., Török, T., Mikić, Z., Linker, J., &
    Murphy, N. A. 2019, ApJ, 887, 103

Ruan, W., Yan, L., & Keppens, R. 2023, ApJ,
    947, 67, doi: 10.3847/1538-4357/ac9b4e

Samanta, T., Tian, H., & Nakariakov, V. M. 2019,
    PhRvL, 123, 035102

Seaton, D. B., & Forbes, T. G. 2009, ApJ, 701, 348

Shen, C., Chen, B., Reeves, K. K., et al. 2022,
    Nature Astronomy, 6, 317

Shen, C., Kong, X., Guo, F., Raymond, J. C., &
    Chen, B. 2018, ApJ, 869, 116

Shen, C. C., Lin, J., & Murphy, N. A. 2011, ApJ,
    737, 14

Shen, C. C., Lin, J., Murphy, N. A., & Raymond,
    J. C. 2013, Physics of Plasmas, 20, 072114

Shiota, D., Isobe, H., Chen, P. F., et al. 2005,
    ApJ, 634, 663

Song, H. Q., Chen, Y., Qiu, J., et al. 2018, ApJL,
    857, L21

Spitzer, L. 1962, Physics of Fully Ionized Gases
    (New York: Interscience)

Stores, M., Jeffrey, N. L. S., & Kontar, E. P. 2021,
    ApJ, 923, 40

Strauss, H. R. 1988, ApJ, 326, 412

Sweet, P. A. 1958, Symposium - International
    Astronomical Union, 6, 123–134,
    doi: 10.1017/S0074180900237704

Takahashi, T., Qiu, J., & Shibata, K. 2017, ApJ,
    848, 102

Takasao, S., & Shibata, K. 2016, ApJ, 823, 150

Titov, V. S., & Démoulin, P. 1999, A&A, 351, 707

Török, T., Kliem, B., & Titov, V. S. 2004, A&A,
    413, L27

Van Doorsselaere, T., Antolin, P., Yuan, D.,
    Reznikova, V., & Magyar, N. 2016, Frontiers in
    Astronomy and Space Sciences, 3, 4

Wang, H., Shen, C., & Lin, J. 2009, ApJ, 700,
    1716

Warren, H. P., Brooks, D. H., Ugarte-Urra, I.,
    et al. 2018, ApJ, 854, 122

Xia, C., Teunissen, J., El Mellah, I., Chané, E., &
    Keppens, R. 2018, ApJS, 234, 30

Xie, X., Mei, Z., Shen, C., et al. 2022, MNRAS,
    509, 406

Ye, J., Cai, Q., Shen, C., et al. 2020, ApJ, 897, 64

—. 2021, ApJ, 909, 45

Ye, J., Shen, C., Raymond, J. C., Lin, J., &
    Ziegler, U. 2019, MNRAS, 482, 588

Zhang, Y., Ye, J., Mei, Z., Li, Y., & Lin, J. 2022,
    Research in Astronomy and Astrophysics, 22,
    085010

Zhao, X., Xia, C., Keppens, R., Mikic, Z., & Gan,
    W. 2017, ApJ, 841, 106

Zharkova, V., & Xia, Q. 2021, Frontiers in
    Astronomy and Space Sciences, 8, 178